Fermi National Accelerator Laboratory

FERMILAB-Pub-92/162
D0 Note 1434

Beam Tests of the D0 Uranium Liquid Argon End Calorimeters

The D0 Collaboration

Fermi National Accelerator Laboratory
P.O. Box 500, Batavia, Illinois 60510

June 1992

Submitted to *Nuclear Instruments and Methods in Physics Research*

Operated by Universities Research Association Inc. under Contract No. DE-AC02-76CHO3000 with the United States Department of Energy

Disclaimer

DØ

Beam Tests of the DØ Uranium Liquid Argon End Calorimeters *

April 15, 1992

The DØ Collaboration

S. Abachi[6], S. Ahn[6], M. Abolins[14], H. Aihara[11], N. Amos[6], Y. Antipov[19], S. H. Aronson[2], R. Astur[14], R. Avellaneda[8], R. E. Avery[17], A. R. Baden[12], B. Baldin[19], J. Bantly[17], E. Barasch[21a], J. F. Bartlett[6], K. Bazizi[4], T. Behnke[21b], V. Bezzubov[19], P. Bhat[6], G. C. Blazey[20], S. Blessing[17], D. Bogert[6], F. Borcherding[6], J. Borders[20], N. Bosko[19], A. D. Bross[6], D. Buchholz[17], N. Bulgakov[19], V. Burtovoy[19], J. M. Butler[6], R. Cence[9], S. Chekulaev[19], S. Cherny[19], J. Chen[1], J. H. Christenson[6], A. R. Clark[11], J. Cochran[22], W. E. Cooper[6], C. Cretsinger[1c], D. Cullen-Vidal[3], D. Cutts[3], O. I. Dahl[11], A. Davidenko[19], K. De[13], M. Demarteau[22], D. Denisov[19], S. Denisov[19], W. Dharmaratna[8], H. T. Diehl[6], M. Diesburg[6], R. Dixon[6], P. Draper[18d], Y. Ducros[21], G. Dugan[6], S. Durston[20], A. Dyakonenkov[19], D. Eartly[6], D. Edmunds[14], A. Efimov[19], J. Ellison[4], R. Engelmann[22], O. Eroshin[19], V. Evdokimov[19], S. Fahey[14], M. Fatyga[2], J. Featherly[2], S. Feher[22], T. Ferbel[20], D. Finley[6], G. Finocchiaro[22], H. E. Fisk[6], G. E. Forden[1], M. Fortner[16], P. Franzini[5], S. Fuess[6], C. S. Gao[6], T. Geld[13], B. G. Gibbard[2], V. Glebov[19], J.-F. Glicenstein[21], B. Gobbi[17], M. Goforth[8], M. L. Good[22], H. A. Gordon[2], N. Graf[6], P. D. Grannis[22], J. Green[16], H. Greenlee[6], P. Grudberg[11], J. A .Guida[22], J. M. Guida[2], W. Guryn[2], N. J. Hadley[12], H. Haggerty[6], S. Hagopian[8], R. Hall[4], D. Hedin[16], T. Heuring[22], R. Hirosky[20], J. Hoftun[3], J. F. Hubbard[21], T. Huehn[4], R. Huson[25], S. Igarashi[6], A. S. Ito[6], M. E. Johnson[6], A. M. Jonckheere[6], K. Johns[1], H. Jostlein[6], W. Karsh[22], S. Kahn[2], A. Kernan[4], L. Kerth[11], A. Kholodenko[19], A. Kirunin[19], E. Kistenev[19], A. Klatchko[4], B. Klima[6], B. Klochkov[19], C. Klopfenstein[22], V. Klyukhin[19], V. Kochetkov[19], W. Kononenko[18], J. Kotcher[15], I. Kotov[19], J. Kourlas[15], E. Kozlovsky[19], S. Kunori[12], S. Krzywdzinski[6], R. Lanou[3], P. Laurens[14], J. Lee-Franzini[22], R. Li[6], Q. Z. Li-Demarteau[22], J. T. Linnemann[14], S. L. Linn[8], R. Lipton[6], F. Lobkowicz[20], S. C. Loken[11], S. Lökös[22], P. Lucas[6], R. J. Madaras[11], R. Madden[8], E. Malamud[6], Ph. Mangeot[21], B. Mansoulié[21], I. Manning[6], H.-S. Mao[6], T. Marshall[10], P. S. Martin[6], H. J. Martin[10], M. Marx[22], A. Mayorov[19], R. McCarthy[22], J. McKinley[14], X. C. Meng[6], K. W. Merritt[6], A. Milder[1], A. Mincer[15], P. Mooney[14], R. Morphis[16], M. Mudan[15], C. T. Murphy[6], F. Nang[3], V.S. Narasimham[23], H. A. Neal[13], P. Nemethy[15], D. Nešić[3], K. Ng[22], D. Norman[12], L. Oesch[13], E. Oltman[11], N. Oshima[6], D. L. Owen[21e], D. P. Owen[14], R. Partridge[3], M. Paterno[22], M. Peters[9], B. Pi[14], H. Piekarz[8], Y. Pischalnikov[19], D. Pizzuto[22], V. Platonov[19], A. Pluquet[21], V. Podstavkov[19], B. G. Pope[14], H. Prosper[6], S. Protopopescu[2], R. Raja[6], S. Rajagopalan[17], L. Rasmussen[22], A. L. Read[6], T. M.-L. Ren[12], S. Repond[16], V. Riadovikov[19], M. Rijssenbeek[22], N. A. Roe[11], P. Rubinov[22], R. Ruland[18], J. Rutherfoord[1], R. D. Schamberger[22], J. Sculli[15], W. Selove[18], A. Shkurenkov[19], M. Shupe[1], W. Smart[6], D. Smith[4], R. P. Smith[6], G. R. Snow[13], A. L. Spadafora[11], R. Stephens[7], , M. L. Stevenson[11], C. Stewart[6], F. Stocker[21f], D. Stoyanova[19], K. Streets[12], M. Strovink[11], A. Suhanov[19], A. Taketani[6], M. Tartaglia[6], J. Teiger[21], G. Theodosiou[18g], J. Thompson[22], S. Tisserant[14], T. G. Trippe[11], P. M. Tuts[5], R. Van Berg[18], A. Vorobiev[19], H. D. Wahl[8], H. Weerts[14], W. A. Wenzel[11], A. P. White[24], J. T. White[25], S. Willis[16], J. A. Wightman[25], S. J. Wimpenny[4], Z. Wolf[7c], J. Womersley[8], Y. Xia[14], P. Xie[6], H. Xu[3], J. Xu[8], R. Yamada[6], P. Yamin[2], J. Yang[15], M.-J. Yang[4h], C. Yoshikawa[9], S. Youssef[8], J. Yu[22], R. Zeller[3], Y. H. Zhou[6], Q. Zhu[15], D. Zieminska[10], A. Zieminski[10], A. Zotov[19], and A. Zylberstejn[21].

---

*Submitted to Nuclear Instruments and Methods in Physics Research.

[1] *University of Arizona, Tucson, AZ 85721*
[2] *Brookhaven National Laboratory, Upton, NY 11973*
[3] *Brown University, Providence, RI 02912*
[4] *University of California, Riverside, CA 92521*
[5] *Columbia University, New York, NY 10027*
[6] *Fermi National Accelerator Laboratory, Batavia IL 60510*
[7] *University of Florida, Gainesville, FL 32312*
[8] *Florida State University, Tallahassee, FL 32306*
[9] *University of Hawaii, Honolulu, HI 96822*
[10] *Indiana University, Bloomington, IN 47401*
[11] *Lawrence Berkeley Laboratory, Berkeley, CA 94720*
[12] *University of Maryland, College Park, MD 20742*
[13] *University of Michigan, Ann Arbor, MI 48109*
[14] *Michigan State University, East Lansing, MI 48824*
[15] *New York University, New York, NY 10003*
[16] *Northern Illinois University, Dekalb, IL 60115*
[17] *Northwestern University, Evanston, IL 60208*
[18] *University of Pennsylvania, Philadelphia, PA 19104*
[19] *Institute of High Energy Physics, 142 284 Protvino, Russia*
[20] *University of Rochester, Rochester, NY 14627*
[21] *CEN-Saclay, 91191 Gif-sur-Yvette, France*
[22] *State University of New York, Stony Brook, NY 11794*
[23] *Tata Institute of Fundamental Research, Bombay 400 005, India*
[24] *University of Texas, Arlington, TX 76019*
[25] *Texas A&M University, College Station, TX 77843*

[a] *Now at 25.*
[b] *Now at DESY, Hamburg, Germany*
[c] *Now at 19.*
[d] *Now at 23.*
[e] *Now at Thinking Machines Inc., Boston, MA*
[f] *Now at SSC Laboratory, Dallas, TX*
[g] *Now at Demokritos, Athens, Greece*
[h] *Now at 6.*

Abstract

We describe the results of beam tests of three uranium-liquid argon calorimeter modules constructed for the DØ detector at the Fermilab Tevatron collider. As part of the calibration procedure, these modules were exposed to beams of electrons, pions and muons between 10 and 150 GeV/c before their installation in the end calorimeter of the completed DØ detector. We obtain an electromagnetic sampling resolution of $15.7\%/\sqrt{E}$ and constant term of 0.3%. The hadronic sampling resolution is $45\%/\sqrt{E}$ (degraded to $50\%/\sqrt{E}$ by the effects of upstream material) and the constant term is 4%. The calorimeter is linear to 0.5%, and the electromagnetic to hadronic response ratio is between 1.02 and 1.09 over this range of momenta. For an electron efficiency of 95% we obtain a rejection factor against pions of $\sim 900 - 3000$ for particles in the momentum range between 50 and 150 GeV/c. We also compare our results with the predictions of a detailed Monte Carlo simulation.

1 Introduction

The recently completed DØ detector is a second-generation device for the study of proton-antiproton collisions at the Fermilab Tevatron collider. One of the design aims of DØ was excellent calorimetry, to provide good energy resolution for electrons, photons and jets, with good overall hermeticity. For these reasons, and for compactness, radiation hardness and uniformity of response, liquid argon with uranium absorber was chosen for the calorimetry. Previous test beam studies were performed to confirm this technical choice[1] and to test electromagnetic and prototype hadronic modules[2].

A cutaway view of the DØ calorimeters is shown in Fig. 1. The system consists of three parts of roughly equal size: a central calorimeter and two end calorimeters. Each of the end calorimeters consists of a ring of 16 outer hadronic (ECOH) calorimeter modules; inside this is another ring of 16 middle hadronic (ECMH) modules; and at the central core is a single large inner hadronic (ECIH) module. The latter weighs 32 tons, has a diameter of 1.7 m and contains approximately 5000 readout channels. In front of the ECIH, and covering the inner part of the ECMH front faces, is a finely segmented electromagnetic calorimeter (ECEM), of 2.2 m diameter, with 7,488 readout channels. Data presented in this paper concern the ECMH, ECIH and ECEM modules.

A necessary part of the program of constructing this detector was the calibration of the calorimeter. To this end, data was taken with these three calorimeter modules in a Fermilab test beam during May–August 1990, before their installation in DØ. The goal was to establish the absolute energy calibration of the calorimeter modules, and to transfer this calibration to DØ. This included the choice of high voltage operating point, effects of possible argon contamination, understanding the resolution of each detector, measuring the uniformity of response over the module (especially in the region of cracks, spacers and edges), and measurements of the shower shape. It also involved comparison with simulations to give confidence that the response of modules not explicitly tested can be modelled accurately. The exercise also served to verify other aspects of the detector system, such as the calorimeter electronics and its calibration, the data acquisition, and the liquid argon purity monitors.

2 Description of the calorimeter modules

The basic construction of the liquid argon calorimeters is shown in Fig. 2. A stack of absorber plates alternates with gaps filled with liquid argon. The shower develops in the dense absorber, and ionization is measured in the argon. The basic sampling cell consists of a depleted uranium absorber plate (4 mm thick in the ECEM, 6 mm thick in the ECIH), a 2.3 mm liquid argon gap, a NEMA G-10 signal board, and another 2.3 mm argon gap. The ECEM and ECIH signal boards are 5 layer printed circuit boards with copper signal pads on the outer surfaces and signal traces on the innermost layer which bring the signals to connectors at the outer radius of the module. Two shielding groundplanes reduce crosstalk to a negligible level. The boards were assembled into disks from 22.5° wedges, and then covered with face-sheet disks of 0.5 mm thick G-10 that had been screen-printed with a thin layer of high resistivity carbon-loaded epoxy. This serves as a positive high voltage electrode; both the signal pads and the absorber plates are at ground potential, the face-sheet serving as a blocking capacitor. The normal operating voltage is 2.5 kV, corresponding to a drift field of 1.1 kV/mm in the gap (see section 6 for a description of the high voltage behavior).

The ECEM electromagnetic calorimeter module[3] provides full azimuthal (ϕ) coverage in the forward direction; ϕ is the angle in the plane perpendicular to the beam. The module covers the polar angle region up to 28° from the beamline (pseudorapidity, $\eta = -\ln\tan(\theta/2) > 1.4$). The module is shown in Fig. 3. It contains 18 sampling cells in depth and has a total thickness of 238 mm (approximately 20 radiation lengths at normal incidence). Signals are read out in four separate longitudinal layers, respectively 2, 2, 6 and 8 sampling gaps in depth (0.3, 2.6, 7.9 and 9.3 radiation lengths). Transverse segmentation is provided by readout pad electrodes on the signal boards, each covering (typically) an η,ϕ interval of $\Delta\eta \times \Delta\phi = 0.1 \times 0.1$. In the third longitudinal layer, which typically contains 65% of the shower energy, the transverse segmentation is made finer, $\Delta\eta \times \Delta\phi = 0.05 \times 0.05$, to provide better shower position resolution. The electrodes are arranged in a semi-projective tower geometry which lines up with that of the ECIH behind. The towers are semi-projective rather than truly projective in that the same pad layout is used for pairs of adjacent readout boards (and for sets of 4 in the last layer) in order to reduce costs. The between-tower boundaries are therefore 'staircases' rather than planes. In order to minimize losses due to internal cracks, the module is built as a monolithic unit. The signal boards and absorber plates are preassembled into disks of approximately 1 m radius and then stacked to assemble the module.

The first two ECEM absorber plates are thin (1.6 mm) stainless steel disks in order to be sensitive to showers initiated in the cryostat walls just upstream (whose thickness is about 2 radiation lengths) and thus to monitor the energy loss therein. The remaining absorber plates are 4 mm thick rolled depleted uranium. The weight of the absorber and signal disks is carried by an aluminum tube around the beampipe. This in turn is supported by a 2cm thick stainless steel strongback in the middle of the module, which is attached to the external mountings. The strongback is followed by a thin steel absorber disk so that the average fraction of energy deposited in the argon for these two cells, as determined by Monte Carlo simulation for 50 GeV/c electrons, is the same as that of a uranium cell.

The hadronic (ECIH and ECMH) modules each contain five longitudinal layers. The first four layers, which are 1.3, 1.2, 1.2 and 1.2 interaction lengths in depth, use fifteen 6 mm thick absorber plates made of uranium – 2% niobium alloy. The fifth layer, which contains an additional 3.6 interaction lengths, uses thirteen absorber plates of 46.5 mm stainless steel for reasons of economy. As in the ECEM, there is a dual 2.3 mm argon gap with a central G-10 signal board between each pair of absorber plates. The uranium absorber plates in the ECIH were made in two semicircles, with alternate plates having the crack between the two halves running horizontally and vertically. In the hadronic modules the semi-projective cells each cover $\Delta\eta \times \Delta\phi = 0.1 \times 0.1$. In the ECIH module, multilayer signal boards are used as in the ECEM; for the smaller ECMH module, surface traces are used to bring out the signals as the distances to the edge of the module are much shorter.

3 Beam test layout

The calibration was carried out in the Neutrino West secondary beam at Fermilab. Figure 4 shows a schematic of the beamline. The beam momentum settings used were between 10 and 150 GeV/c. The beam polarity was negative, and particles available were π^-, e^- and μ^-. The electron beam was produced using a lead sheet to convert photons from neutral pion decays, while the muon beam used a beam dump to absorb all secondary particles except muons. The beam was operated in slow spill mode over a 22 s interval, with the instantaneous rate normally restricted to a few thousand particles per second (to limit the effects of pileup in the calorimeter). The beam at the calorimeter had a momentum spread of 1.1% and approximately Gaussian profiles, with width $\sigma = 1.5$ cm horizontally and 1.1 cm vertically. The beamline was instrumented with scintillation counters to form the beam trigger. Proportional wire counters with 1 mm wire spacing were provided for reconstruction of beam particle trajectory and momentum, and two threshold Čerenkov counters were used for electron identification.

The calorimeter modules to be tested were enclosed within a double-walled liquid argon cryostat vessel. The cryostat was cylindrical, approximately 3 m in diameter and 5 m long. It was mounted on a motorized transporter system able to move the vessel through the following ranges of motion:

- 190° rotation about a vertical axis
- ±15° rotation about the horizontal long axis of the cylinder
- 3.5 m horizontal translation perpendicular to the beam
- 0.75m vertical translation.

These motions were sufficient to allow the beam to be directed into the modules along the trajectory that would be followed by particles from the DØ interaction point, over a range of pseudorapidity, azimuthal angle, and interaction point positions within the beam crossing. A PC-based control system was used to drive the transporter; the operator could enter the desired position in the DØ coordinate system, and the required motion on each of the four motors would be calculated and executed. The transporter also enabled the cryostat to be positioned for loading of the modules into the cryostat through one end. The beam entered the cryostat through a thin end window consisting of two 1.6 mm steel plates.

The cryogenic system supplied the cryostat with high purity liquid argon and with liquid nitrogen for cooling purposes. The system maintained the temperature within ± 1 K of the nominal 90 K and the pressure within ±0.5 psi of the nominal 20 psi(a). Cooldown of the calorimeter modules took about 4 days and was monitored with approximately 70 resistive temperature sensors mounted on the cryostat and within the modules.

The arrangement of the modules within the cryostat is shown in Fig. 5. It should be noted that the ECEM and ECIH modules were in the correct relationship to each other, and that extra material in the form of aluminum and steel plates was included to mock up the material that will be present upstream of them in the full DØ detector. This consisted of a foamed plastic argon excluder, a 2.5 cm thick steel plate to simulate the EC cryostat walls, and a 4.4 cm thick aluminum plate at small angles to simulate the vertex detector end plates and electronics.

Behind the ECIH, an ECMH module was mounted also on the beam axis, which is not its position in the full DØ detector. This enabled measurements to be made of the amount of shower energy leaking from the ECIH down the beam pipe, and it was also exposed directly to electron and pion beams passing through the simulated DØ beam pipe. This was a 5 cm diameter stainless steel tube, filled with helium gas to reduce the amount of material upstream of the ECMH.

The instrumented region in the module array covered approximately 60° in azimuth, together with all azimuths for the region around the beampipe. This was large enough for hadronic shower containment and allowed the beam to be scanned over various areas of interest in the modules. Approximately 1450 ECEM channels, 2400 ECIH channels and 120 ECMH channels were read out. This represents about 10% of the total number of calorimeter channels in the full DØ detector.

4 Monte Carlo simulation

In order to verify our understanding of the calorimeter bahavior, a comprehensive simulation effort was undertaken using the CERN Monte Carlo program GEANT[4]. This program provides a framework for tracking particles through the detector geometry and simulating physics processes of the shower. The detector geometry was modelled in considerable detail, including individual uranium plates, argon gaps and readout boards throughout the modules, the correct materials upstream of the calorimeters including beamline instrumentation, and the cryostat vessels. Tracking in the resulting detailed geometry is slow because of the many independent volumes involved; nevertheless, for single-particle test-beam events, the time taken (of the order of 24 minutes to simulate a 50 GeV/c incident pion using a DEC VAXstation 3100-M76) was considered tolerable.

The GEANT geometry was created from text files describing the detectors, using a DØ-developed geometry-building program[5]. The Monte Carlo program itself was designed to share a common framework with the full DØ detector Monte Carlo, with different options selected by the user at link time. This package of tools for the use of GEANT will be described in more detail in a future paper. Version 3.14 of GEANT was used, with the tracking carried down to 10 keV for electromagnetically interacting particles and 100 keV for hadronic particles. The output events were in the same format as real data and could be read with the same programs, facilitating analysis and comparisons.

5 Electronics and calibration

A crucial aspect in establishing the absolute calibration of the DØ calorimeter is the understanding of the performance of the calorimeter electronics.

5.1 Detector electronics

The calorimeter signals are brought out of the cryostat through feedthrough ports. Inside the cryostat the signals are ordered so that physically close towers are close to each other on the cables. This allows signals from many η, ϕ towers from a particular depth to appear on a single multiconductor cable. The signals are reordered in the feedthrough ports so that all the readout cells of a $\Delta\eta \times \Delta\phi = 0.2 \times 0.2$ semi-projective tower exit on two adjacent multiconductor cables, facilitating the formation of a fast trigger. Short runs of cables connect the external side of the feedthrough to low noise hybrid charge-sensitive amplifiers (preamps). Two versions of preamps are used, one with a $5pF$ and one with a $10pF$ feedback capacitor. The $10pF$ version is used in layers 3 and 4 of the electromagnetic section of the calorimeter, where the largest signals occur.

The output voltages of the preamps are fed into a shaping and sampling circuit, known as the base line subtractor (BLS) [6]. The shaping in the front end of the BLS hybrid consists of a $430ns$ integration and a $33\mu s$ differentiation. In addition, there is a gain of 3 to change the full scale from 3.3 volts at the preamp output to 10 Volts at the sampling stage. The shaped signals peak between 2 and $2.4\mu s$, depending on the detector capacitance, and have a broad maximum around $2.2\mu s$. Baseline subtraction from dual sampling follows the shaping. Two analog memory cells follow the signal until a trigger is received from the counters in the beam. On arrival of this trigger, one memory cell samples the delayed calorimeter signal before it has begun to rise, forming the baseline sample. The second memory cell holds the signal $2.2\mu s$ later, to form the peak sample. The difference between the peak and the baseline is sent to the ADC.

Fifteen bit dynamic range is obtained with low cost 12 bit successive approximation ADCs by using precision ×8-or-×1 amplifiers, whose gains can be forced into either of the two values, or selected automatically according to the signal amplitude. If the difference signal reaching these amplifiers is less than 1.25 V, it is amplified eightfold and the result digitized by the 12 bit ADC circuitry. Larger signals are digitized directly, with no additional analog gain, and the resulting ADC output digitally shifted by 3 bits [6].

The ADCs digitize 24 input signals simultaneously in about $10\mu s$, and repeat this cycle 16 times to complete digitizing all 16×24 channels in one ADC card. Because of the ×8-or-×1 amplification, the dynamic range of the measurements is 2^{15}. The ADCs reside in a VME crate that reads the outputs into a VME buffer, which drives the data cable. The data cable carries the data to the dual-port memories of a set of four DEC MicroVAX-II computers.

The ADCs can perform pedestal subtraction and zero-suppression separately for each channel, though in fact these functions were performed offline during this test-beam run. During the whole running period, pedestal and pulser runs were taken on a regular basis. The pedestals were stable to within 1 ADC count (0.4% of a typical pedestal).

5.2 Noise

The performance of a system with a very large number of electronic channels can be severely affected by the presence of noise. Consider the variance S^2 of the signal obtained by summing N channels (to measure total energy, for example). For simplicity we can assume that each channel has the same random noise σ^2 and that there is a cross-correlation c^2 between pairs of channels. Then

$$S^2 = N\sigma^2 + N(N-1)c^2. \tag{1}$$

As N becomes large, the random noise σ^2 must be kept low to obtain a reliable measurement. The second term, $N(N-1)c^2$ grows even faster; this is the so-called "coherent noise", in which channels tend to fluctuate together. The coherent and random noise become equal when $N = \sigma^2/c^2$ channels are added together, so it is necessary to ensure that the coherent noise remains small or else it will dominate. The DØ electronics system is designed to ensure that both random and coherent noise remain manageably low.

The rms noise voltage measured by the ADC is proportional to the noise density and the bandwidth of the system, and is linear in the total detector cell capacitance [7][8]. Fig. 6(a) shows the distribution of the standard deviations of the pedestals, taken in the ×8-mode, versus the detector cell capacitance C_D, for the case where the high voltage on the signal boards is turned off (and hence there are no signals from uranium radioactivity). The linear dependence on the detector cell capacitance can be seen quite clearly. This dependence arises because the amplifier noise consists of an (equivalent) series voltage source and a parallel current source at the amplifier input. The voltage source supplies an amount of charge proportional to the detector cell capacitance, accounting for the linear slope, while the current source supplies a constant charge which accounts for the offset at $C_D = 0$. The random noise per channel corresponds to about 150-200μV at the preamp output. It should be noted that 100μV correspond to approximately one ADC count, which represents a charge of 3000 electrons at the preamp input. Fig. 6(b) shows the same scatter plot with the high voltage applied to the signal boards. The broadening of the distribution is due to the uranium noise. It is interesting to note that for some channels the pedestal width is the same for both cases. These channels, typically the channels with a large capacitance, are the readout channels of the coarse sections of the calorimeter modules that use stainless steel rather than uranium as absorber.

In order to understand the effect of radioactive decays of uranium on pedestal distributions, a simple Monte Carlo was written which simulates pileup of minimum ionizing particles in the liquid argon gaps. In this study, it was assumed that all effects may be simulated using only minimum ionizing particles. The current induced in an argon gap by uranium activity is well established at 4 pA per cm^2 of uranium surface, which may be converted to a mean time between decays, τ. This depends only on the amount of uranium surface area that is exposed. Using this time distribution for radioactive decays, a uranium noise spectrum was generated by assuming that the signal amplitude was the same as that of cosmic rays, but that the time relative to the trigger was random. The known time dependence of the calorimeter pulse after shaping was used to derive the signal. This uranium noise signal is non-Gaussian because the calorimeter pulse has an asymmetric time dependence. In addition to this uranium noise, there is a capacitance noise from the amplifiers, which is Gaussian. The convolution of these distributions is shown in Fig. 7, superimposed upon the measured pedestal distribution of a central tower. The agreement is excellent.

Much effort was spent grounding and shielding the preamplifier/BLS system to minimize coherent noise from oscillations, pickup and crosstalk; all detected sources were eliminated. The level of coherent noise is consistent with zero; an upper limit based purely on the measurement precision is 5-7μV per channel. This corresponds to a charge of about 150 electrons per channel at the preamp input. These measurements were repeated at the full D0 detector, with a factor two higher precision, and again most channels showed no coherent noise at the threshold of sensitivity. The number of channels that can be added before the coherent noise starts to dominate is thus at least 2000 channels. A typical electron shower contains 100 cells with signals above the zero-suppression threshold; a hadron shower, 400. The noise is low enough to permit minimum ionizing particles to be detected unambiguously in the calorimeter (see section 10). The signal for a minimum ionizing particle is about 10 ADC counts per centimeter of liquid argon.

5.3 Gain calibration

A precision resistor (0.1% tolerance) is connected to the input of each preamp channel. This allows measurement of the relative response of all channels using a pulser system [8][9], which consists of a current source, an attenuator box (to control the amplitude of the injected charge) and a coaxial switch box. During a pulser calibration run the system steps through 32 switch positions of the switch box, with a pattern of 144 channels available at each position of the switch.

Given an input voltage $V(t)$ at the input to the preamp, the output voltage is given approximately (see Fig. 8) by:

$$V_{out} = \frac{\int V(t)dt}{RC_F} \frac{AC_F}{AC_F + C_D} \tag{2}$$

where C_F is the feedback capacitance, C_D the detector capacitance, R is a resistance in series with the pulser, and A is the DC open-loop gain of the preamp. To ensure an equal response for all channels, $R = 499k\Omega$ and $249k\Omega$ were used for the $C_F = 5$ pF and 10 pF channels respectively. The detector capacitance C_D ranges from 1.5 to 5.0 nF, and the open loop gain $A \approx 5000$. The width of the pulse from the pulser is about 300 ns. The uniformity of the pulser distribution for all channels has been measured to be better than 0.25%, with an rms of about 0.1%. The relative timing accuracy in the full system will be ±10 ns, with a combined error from all sources on the measured gain of $< 0.2\%$.

The pulses are digitized and analyzed online and two gains are obtained for each channel, corresponding to the ×1 and ×8 amplifier settings.

The linearity of the gains was studied using pulser runs taken at a series of attenuator settings. The output ADC values, corrected for the detector and feedback capacitance as given above, were fitted to straight lines for both the ×1 and ×8 amplification regions. The results for a typical channel are shown in Fig. 9. Plotted here is the ADC output versus pulser amplitude. The pulser covers an energy range from 2.5 to $50 GeV$. The deviations from a straight line fit for all channels are less than ±0.25%, and the channel-to-channel relative response for a given pulser amplitude has an rms spread of $\approx 2.3\%$.

Events from a single pulser pattern of 144 channels were used to study gain stability. The rms gain variation over time is about 0.8%. To remove temperature dependences, a linear correction[8] was applied to the gains. The BLS and preamp crate temperatures were read out and recorded at the start of each run. With the BLS and preamp temperature correction, the variation of the gains is reduced by about a factor of four. Fig. 10 shows the time dependence of the gain of a particular channel, normalized to the average gain for the 144 channels in this pulser pattern, after the temperature corrections.

6 High voltage behavior

Argon purity was monitored using ionization cells, in which a radioactive source creates ionization in an argon gap. The complete purity monitoring system, described in detail elsewhere[11], included eight test cells, located in pairs at four different locations within the test cryostat. Each pair included an α test cell and a β test cell. The α test cell has a single 2.3 mm argon gap with an ^{241}Am source electro-deposited on a conducting plane. The gap size is the same as that used in the DØ calorimeter. The electrons freed from the argon by the ionizing α particles are collected and the resultant signal amplified. The strength of the signal depends on argon purity and high voltage. The argon purity can be deduced from the shape of the response as a function of high voltage. The β test cell has two gaps. The first gap contains an electro-deposited ^{106}Ru source, and is used to collect the electron ionization signal when triggered by a signal in the second gap.

The response of the test cells was monitored continuously during the 1990 run. Table 1 lists the percentage change R(α) in the various α cell responses at a field of 13 kV/cm over the entire running period. The errors differ between the four cells because of variation in the local noise characteristics of the sensor and preamplifier. A weighted average of the four channels shows less than 0.25% signal loss at the 95% confidence level.

The table also shows the percentage changes, R(β), in the ratio of β cell response at a field of 0.8 kV/cm to the response at 10.9 kV/cm, for three of the four β cells (the fourth developed a problem at the start of the run). Because ^{106}Ru has a short half-life (1.020 years), the pile-up rate from the source changes over the course of an experiment. Since pile-up significantly affects the response, the ratio is used to minimize the effect. A decrease of 0.9% in R(β) was seen during the run. Test cell results with varying oxygen contaminations indicate that such a decrease corresponds to less than a 0.1% signal loss at 10.9 kV/cm[11]. Since the calorimeter and the β cells have similiar response (see Fig. 11), the loss in the calorimeter response to electrons is also less than 0.1%. Comparison of α and β response to various oxygen contaminations indicates that a loss of 0.25% in α signal at 13.0 kV/cm corresponds to less than a 0.1% loss in β signal at 10.9 kV/cm. This is in agreement with the loss deduced from the β ratio. Direct measurements showed that the detectors were stable to better than 0.3% at the operating voltage of 10.9 kV/cm during the duration of the run.

In later tests we have made direct comparisons between the response of the monitors and the detector response for known argon contamination levels. This will be reported in a subsequent paper.

Figure 11 shows the calorimeter response to 100 GeV/c electrons as a function of calorimeter voltage. Also shown is the response of an argon β test cell. Both sets of measurements have been normalized to the response at 13.0 kV/cm. The rise to the plateau for both curves is sharper than observed during previous test beam runs. The response of the β test cell tracks quite closely with the electron response. The shape of the β response indicates that the effective oxygen content of the LAr is less that 1.0 ppm[12].

Sensor	R(α)%	R(β) %
1 α	-0.05 ± 0.11	—
2 α	$+0.25 \pm 0.89$	—
3 α	-0.31 ± 0.13	—
4 α	-0.05 ± 0.11	—
All α	-0.12 ± 0.07	—
1 β	—	-1.2 ± 0.5
2 β	—	-0.9 ± 0.1
3 β	—	-0.8 ± 0.5
All β	—	-0.9 ± 0.1

Table 1: Change in α and β-cell response over the 100 day run.

7 Electromagnetic response and resolution

7.1 Electron response as a function of energy

A series of runs were taken with electron beams of momenta ranging from 10 to 150 GeV/c to study the calorimeter linearity and energy resolution. For this analysis, events were required to have a beam track reconstructed by the PWC system and to be flagged as an electron by the Čerenkov counters.

The energy of electromagnetic showers was reconstructed by summing the four longitudinal sections in the ECEM and the first section of the ECIH for an $n \times n$ array of 0.1×0.1 pseudo-projective towers. The number of towers summed to contain an electromagnetic shower varies with η, corresponding to the variation of pad size with η. At $\eta = 1.95$, the location where the energy resolution was determined, 99.6% containment is achieved by summing an array of 5 by 5 towers. Channels were required to have signals outside a symmetric threshold around zero ($\pm 1\times$ r.m.s. noise). Each channel was pedestal-subtracted and corrected for electronic gain.

The reconstructed energy (in GeV) for event i is given by:

$$E_i = \alpha \sum_{j=1}^{5} \beta_j ADC_{ji} + \delta \tag{3}$$

where a weight, β_j, is given to the ADC counts of each readout layer. The third layer weight, β_3, is set equal to 1 and α is an overall scale factor. The additive term,

δ, is a small offset which can be attributed to energy loss before the calorimeter, and is determined from the data. The ratios of the inverse sampling fractions for each layer, as calculated from the dE/dx values for minimum ionizing particles (see Table 2), can be used as the first-approximation layer weights in Eq. 3. (The sampling fraction is defined as the fraction of a particle's energy that is deposited in the sensitive medium, liquid argon in our case.) An improved set of weights is obtained from the data by minimizing the deviation of the reconstructed energy from the track momentum measured by the PWC system, i.e. minimizing:

$$\chi^2 = \sum_{k=1}^{7} \sum_{i=1}^{N_k} \frac{(p_i - E_i)^2}{\sigma_i^2} \tag{4}$$

where p_i is the measured PWC track momentum for event i, the first sum is over the seven runs with beam momenta ranging from 10 to 150 GeV/c, and the second sum is over the N_k events of any run with a given momentum setting. An equal number of events (1000) at each momentum setting is used to obtain weights which are optimized uniformly over the momentum range. The estimated measurement error, σ_i, used in calculating the χ^2, is taken from a fit to the resolution given below.

The optimized layer weights, given in the last column of Table 2, are consistent with the ratios calculated from minimum ionizing dE/dX losses, except for the first layer. Although this first layer has a "low mass" construction (using 1.6 mm steel plates in place of 4 mm uranium absorber plates), its effective sampling fraction is low because of the inclusion of material upstream of the detector, used to simulate the cryostat walls at the collider. The optimized fit yields an overall scale factor $\alpha = (3.74 \pm 0.01) \times 10^{-3}$ GeV/ADC and an offset $\delta = 0.30 \pm 0.02$ GeV.

The distribution of reconstructed energy for runs of various beam momenta is shown in Fig. 12. The 1.1% spread in the beam momentum was corrected event-by-event using the momentum measured (to an accuracy of ±0.2%) by the PWC system.

The linearity of the calorimeter's response can be seen in Fig. 13(a) which shows the agreement of the mean of a Gaussian fit to the reconstructed energy with the mean track momentum for the various beam momentum settings. Over the momentum range studied, the deviations from linearity are less than ±0.3%.

The fractional energy resolution, calculated as σ/E, where σ and E are the standard deviation and mean from the Gaussian fits, is shown in Fig. 13(b).

	dE/dx		Fit
Layer	SF	$\frac{SF(3)}{SF(i)}$	β_j
EM1	.049	1.83	$1.47 \pm .03$
EM2	.088	1.01	$1.00 \pm .01$
EM3	.089	1.00	(1.0)
EM4	.081	1.10	$1.10 \pm .01$
IH1	.053	1.67	(1.67)

Table 2:

The sampling fractions (SF) calculated for a minimum ionizing particle, these values normalized to the third EM layer ($SF(3)/SF(i)$), and the layer weights (β_j) found from the resolution/linearity minimization. The dE/dx values for the first readout layer (EM1) include the material upstream of the module. The values in parentheses were not varied in the fit.

We assume the energy dependence of the resolution is of the quadratic form:

$$\left(\frac{\sigma}{E}\right)^2 = C^2 + \frac{S^2}{p} + \frac{N^2}{p^2} \tag{5}$$

where p is the beam momentum in GeV/c, C is a constant contribution from systematic errors such as remaining channel-to-channel variation in gain, S is due to the statistical error in sampling, and N represents energy independent contributions to σ such as electronic and uranium noise. The results of the fit are:

$$\begin{aligned} C &= 0.003 \pm 0.003, \\ S &= 0.157 \pm 0.006(\sqrt{\mathrm{GeV}}), \text{ and} \\ N &= 0.29 \pm 0.03(\mathrm{GeV}). \end{aligned}$$

The noise term, N, is consistent with the value obtained from pedestal widths for an array of 5 × 5 towers.

7.2 Position resolution

The transverse spread of an electromagnetic shower, which results in sharing of the energy among several towers, enables the centroid of the shower to be determined with much better accuracy than one would naively calculate on the basis of the calorimeter segmentation. In the ECEM, the shower position can be most accurately determined in the third longitudinal section (EM3), which has a transverse segmentation of 0.05×0.05 in $\eta \times \phi$. We have studied the position resolution in EM3 using the entry position of the particle as extrapolated from the PWC's in the beamline. Several techniques are available to extract the point of origin of an electromagnetic shower; we have studied two algorithms, both of which give very satisfactory results.

In the first method, the transverse shower shape is fit to the sum of two exponentials and a ratio of observed energies is constructed, from which the shower impact position can be determined iteratively[3]. In the second method[13], a first estimate of the position is made by calculating the energy weighted center-of-gravity, $X_{COG} = \sum X_i E_i / \sum E_i$, and then correcting it using the following algorithm:

$$X'_{COG} = X_m + B \cdot \sinh^{-1}\{\frac{(X_{COG} - X_m)}{\Delta} \cdot \sinh(\frac{\Delta}{B})\}. \tag{6}$$

In this expression, X_m is the position of the EM3 tower with the largest signal, Δ is the pad half-width and B characterizes the transverse shower shape assuming a (single) exponential dependence on transverse distance.

The position resolution as determined by these two techniques was very similar. In both cases, the best resolution is obtained when the shower originates near the edge of a tower, and gets worse as the square of the distance from the tower edge. In addition, owing to the inherently statistical nature of shower development we expect the position resolution to vary approximately as $1/\sqrt{E}$. In Fig. 14 the position resolution obtained using the corrected center-of-gravity technique is shown as a function of energy. Both the resolution at the tower edge, and the resolution integrated over the tower width at η=1.95 (where the pad size in EM3 is 2.6 cm) are shown. The former does vary approximately as $1/\sqrt{E}$ while the average resolution shows a slightly stronger dependence. The average resolution is approximately 2 mm at 25 GeV/c and 1 mm at 75 GeV/c.

8 Pion response and resolution

The resolution and linearity of the inner hadronic calorimeter were evaluated using data from 10 to 150 GeV/c, taken at $\eta = 2.55$, where shower containment is maximal. All instrumented channels in the ECIH and ECEM, with signals outside a symmetric threshold around zero (±2× r.m.s. noise) were included in the total energy sum. Each channel was pedestal-subtracted and corrected for electronic gain. Data were also corrected for the spread in the beam momentum on an event by event basis.

8.1 Pion Response as a Function of Energy

Cuts were imposed requiring a single good beam track, no evidence of pileup from previous events, and no signal in the muon and halo counters. In addition, data were analyzed both with and without a cut requiring less than 150 ADC counts (0.51 GeV energy) in the EM1 layer. This cut was intended to remove events in which an interaction had occured in the material upstream of the calorimeter. This material was included in the test beam to simulate the material in the DØ cryostat and vertex chamber. Results which include the EM1 cut can be regarded as providing a measure of the intrinsic resolution of the calorimeter while results without the cut are a closer approximation to the performance expected at DØ, though a correction for early showering should ameliorate the resolution broadening. Figure 15 shows the calorimeter response to 100 GeV/c pions both with and without the EM1 cut.

Energies measured in each layer i were multiplied by the (relative) weight β_i for that layer. The weights for the EM section were taken from electron studies (section 7) and, as before, β_3 (for EM3) was fixed at 1.0. Weights for the hadronic layers were obtained in two ways. The first set (dE/dx weights) was calculated by assuming that the energy loss was proportional to that of a minimum ionizing particle. The second set of weights was obtained by minimizing the resolution, subject to a constraint of linearity, over the entire energy scan by varying three ECIH weights (IH1,IH2-4,and IH5) relative to the ECEM weights. The results of this study are shown in Table 3. The remainder of this analysis will use the final fitted weights. Results using the dE/dx weights have only slightly worse resolution than those using the fitted weights. Data at each energy were fitted to a Gaussian. As Fig. 15 suggests, non-Gaussian tails which would be caused by a different intrinsic response to electromagnetic and hadronic energy deposition (i.e. a non-unity value of e/h) are small.

Figure 16 shows the deviations from a linear fit to the mean pion pulse height as a function of beam momentum. The fit gives an overall scale factor of $\alpha = (3.89 \pm 0.01) \times 10^{-3}$ GeV/ADC and an offset $\delta = -2.20 \pm 0.05$ GeV. The residuals to a linear fit are in all cases smaller than 3% and are typically less than 0.5%. The increased offset relative to the electron data is probably due to some nonlinearity at the lowest energy point (10 GeV) apparent from the figure. This is

Layer	dE/dx weight	Fitted weight
IH1	1.63	1.57
IH2–4	1.54	1.55
IH5	5.72	5.56

Table 3: Layer weights determined from dE/dx and from fitting, for the ECIH module.

consistent with the observed increase in the e/π ratio at this energy (see the next section).

The pion resolution is parameterized as before, as $(\sigma/\mu)^2 = C^2 + S^2/p + N^2/p^2$ where N,S, and C are the noise, sampling, and constant term contributions to the resolution and p the measured momentum of the beam particle. The noise term was evaluated, using pedestal data, to be 975 MeV. Figure 17 shows resolutions for data both with and without the EM1 cut. We find an intrinsic sampling resolution of $0.45\sqrt{\text{GeV}}$, which degrades to $0.50\sqrt{\text{GeV}}$ if the EM1 cut is removed. Our measured sampling term is consistent with expectations based on calculations by Wigmans[14]. Our resolution is also well described by a GEANT simulation of the calorimeter. We estimate that at most 1% of the $3.5 - -4\%$ constant term can be attributed to improper gain calibration and 1% may be due to the departure of e/h from unity. An additional 1–2% may be due to lack of complete containment of the showers[15].

Data from the ECMH module suffered from the presence of additional upstream material, which caused a low energy tail in the observed energy distribution, as shown in Figure 18. This effect was parametrized by convoluting the usual Gaussian response of the detector with an exponential term representing upstream energy loss. The exponential has a width λ, where λ is the average upstream loss in ADC counts. The ECMH pion energy response was fitted to:

$$f(x) = \frac{N}{\lambda\sigma\sqrt{2\pi}} \int_0^{\mu} \exp\frac{\mu - y}{\lambda} \exp\frac{-(x-y)^2}{2\sigma^2}\, dy \tag{7}$$

where μ and σ, extracted from the fit, are taken to be the mean and width of the Gaussian response which the ECMH detector would have had in the absence of upstream energy loss.

In Fig. 19, the ECMH resolution is shown for both electrons and pions. For pion showers, the sampling term of 0.41 ± 0.04 $\sqrt{\text{GeV}}$ compares well with that found in the ECIH data. For electromagnetic showers, a sampling term of 0.19 ± 0.02 $\sqrt{\text{GeV}}$ is consistent with the value found in the ECEM module scaled by the square root of the ratio of sampling fractions. Table 4 summarizes our results for the ECIH and ECMH modules for the various analyses.

Detector	Weighting	Sampling Term (S)	Constant Term (C)
ECIH pions	dE/dx	0.546 ± 0.008	$0.041 \pm .001$
ECIH pions	Fitted	0.501 ± 0.008	$0.044 \pm .001$
ECIH pions, EM1 cut	Fitted	0.446 ± 0.009	0.039 ± 0.002
ECMH pions	dE/dx	0.41 ± 0.04	0.032 ± 0.004
ECMH electrons	dE/dx	0.19 ± 0.02	0.008 ± 0.004

Table 4: Hadronic and electromagnetic energy resolutions in the ECEM+ECIH and in the ECMH modules.

8.2 Electromagnetic to hadronic response ratio e/π

Our previous studies[2] showed that a uranium-liquid argon calorimeter can be made nearly compensating, i.e. the ratio of electromagnetic and hadronic response at any energy (e/π) is close to unity. In order to measure e/π for the present calorimeter modules, we compared the response for electrons and negative pions at $\eta = 2.55$, at the ECIH benchmark. To measure e/π without introducing systematic errors one needs to make the analysis as similar as possible for electrons and pions. We therefore sum the same channels in each case, adding many more channels than is usual for electron data, and thus become sensitive to possible systematic pedestal offsets. For this analysis the pedestals were not subtracted using the standard pedestal files, but pedestal events interspersed between the beam events were used instead, so that effects due to pileup from out of time events would affect pedestals and data in the same way. The electron and pion data were both summed within 15 × 15 towers around the beam. The pion data were additionally required to have the energy in the first EM layer to be less than some value, in order to remove events where the shower started upstream of the detector. In the e/π analysis this EM1 cut was relaxed to 1.2 GeV in order to improve the statistics. The e/π ratio is plotted in Fig. 20(a). The uncertainties on the data points include (and in some cases are dominated by) the statistical uncertainty from the pedestal subtraction, because of the limited number of pedestal events. The e/π ratio is about 1.16 at 10 GeV/c and falls to 1.06 at 150 GeV/c. Also plotted are the predictions of two alternative hadron shower algorithms GHEISHA[16] and NUCRIN[17], each run within the framework of the GEANT 3.14 Monte Carlo. It can be seen that GHEISHA reproduces rather well the observed trend of e/π, but the NUCRIN prediction is too high. These Monte Carlo calculations were done assuming that the charge produced in the liquid argon is proportional to the energy deposited therein, thus ignoring possible saturation effects in charge production by any heavily ionizing particles.

In Fig. 20(b) the data and Monte Carlo are again plotted, this time using the GEANT/GHEISHA Monte Carlo to correct the data for the energy leaking outside the instrumented region of the calorimeter, and for the effect of the cut on the EM1 layer. This therefore shows the e/π ratio that would be expected for the sum of all channels in a fully instrumented calorimeter and no material except the cryostat upstream. The size of the Monte Carlo corrections is typically 3–6%. The errors on the data include a systematic uncertainty in these corrections from the limited statistics of the Monte Carlo events. They also include a 0.5% uncertainty on the leakage correction for energy oustide the instrumented area. This is estimated from the level of agreement between the data and Monte Carlo in describing the fraction of hadron shower energy contained within a transverse window ranging from 8×8 to 18×18 towers. We have not corrected the results for downstream leakage. Also plotted are results from the GEANT/GHEISHA Monte Carlo, as before; the agreement between the data and Monte Carlo is quite good.

We have compared these results with the predictions of Wigmans[14]. Using his parameterization of $f_{EM} = 0.1 \ln E(\mathrm{GeV})$ for the electromagnetic fraction in a hadronic shower between 10 and 100 GeV, we can derive the 'intrinsic e/h' of the calorimeter, that is the ratio of its sensitivity to electromagnetic and hadronic forms of energy deposition. The result varies from $e/h = 1.12$ at 10 GeV/c to $e/h = 1.04$ at 100 GeV/c (ignoring the 150 GeV/c point because it is outside the validity of the parameterization and has leakage of the order of a few percent). This is reasonably consistent with Wigmans' predictions, which are that $e/h = 1.10$ for the 4 mm thickness of uranium in the ECEM and 1.08 for the 6 mm uranium thickness in the ECIH.

As an additional measure of the electromagnetic to hadronic response ratio, we selected "EM showers" in the ECIH hadronic module by requiring events to have over 90% of their energy in any single layer of the calorimeter (30 radiation lengths). This selects hadronic showers which are very electromagnetic in character. From 187 events passing the cut, one obtains a response ratio "π^0/π"$=$ 1.094 ± 0.005 at 100 GeV/c. This was compared with the GEANT/GHEISHA

Monte Carlo by inserting single π^0's into the calorimeter at the start of a hadronic layer. The Monte Carlo predicts "π^0/π"$= 1.117 \pm 0.008$ at 100 GeV/c, which is in good agreement with the data.

8.3 Longitudinal development of pion showers

Figure 21 shows the energy deposited in two typical layers of the calorimeter (the plot is for 100 GeV/c pions in the third ECEM layer and the first ECIH hadronic layer). The dashed distributions are for the GEANT/GHEISHA Monte Carlo, and reproduce the data very well.

Figure 22 shows the mean energy deposited in each layer of the calorimeter for 50, 75, 100 and 150 GeV/c incident pions. Upstream interactions were minimized by cutting on the energy in the first layer of the electromagnetic section of the calorimeter. These distributions are also well reproduced by the GEANT/GHEISHA Monte Carlo, as shown in the figure.

The longitudinal development of pion showers was fitted to the usual parameterization of Bock et al.[18]. The energy δE deposited in a small interval of δs radiation lengths and δt interaction lengths, a distance s radiation lengths and t interaction lengths from the start of the shower, is given by:

$$\delta E = \frac{E_0}{\Gamma(a)}\, w\, (bs)^{a-1}\, e^{-bs}\, b\, \delta s + \frac{E_0}{\Gamma(c)}\, (1-w)\, (td)^{c-1}\, e^{-td}\, d\, \delta t \qquad (8)$$

where Γ is the gamma function, E_0 the incident energy, and a,b, c, d, and w are the parameters fitted. This form was fitted to 50, 75, and 100 GeV/c pion data, after introducing fluctuations in the origin of the shower and in the effective values of s and t[19]. The following were the results of the fit:

$$\begin{aligned} a &= c = 0.316 + 0.361 \ln(E) \\ b &= 0.20 \\ d &= 1.03 \\ w &= 0.43 \end{aligned}$$

Figure 22 shows that the parametrization well reproduces the distribution of energy between the calorimeter layers.

The parameterization also provides a good description of the lack of containment of pion showers when they do not pass through the full calorimeter. The energy response to 100 GeV/c pions for various values of pseudorapidity is shown in Fig. 23, together with the response expected from the parameterization (obtained by integrating the form of Eqn. (8) up to where the shower exited from the detector). The data and the parameterization compare well, considering that transverse shower shape has not been incorporated. (It should be noted that the transverse leakage does not occur for the full DØ calorimeter which has full solid angle coverage).

8.4 Rate dependence of response

Because the energy resolution of the hadronic calorimeter was observed to degrade at high beam intensities, a study was performed to evaluate the rate dependence of the resolution. The DØ pulse shape is characterized by a fast rise ($\sim 2\mu s$) and a slow fall ($\sim 50\mu s$), with 2.2 μs base-peak sampling. Because of this shape, there is a much higher probability of sampling the falling edge of a preceding pulse rather than the rising edge of a following pulse when there is pileup. This means that pileup noise from random out-of-time pulses usually produces a large number of small negative signals from the falling edge together with a few large positive signals from the rising edge. This broadens the resolution.

A series of ten 150 GeV/c pion runs were taken at intensities varying from 2.8×10^4 to 1.62×10^6 particles per 20 second spill. The data were obtained for a fixed pseudorapidity of 2.3, with 3000 events per run. The energy resolution, obtained from a Gaussian fit to the reconstructed energy, as a function of rate is shown in Fig. 24. The results indicate a degradation of about a factor of two from lowest to highest intensity, with the resolution changing from 5.5% to 10.5%. It is also evident from Fig. 24 that, below a rate of 5 kHz, there is very little rate-dependence to the resolution. At the highest intensities, distributions in the total observed energy, as well as the pedestals taken during the spill, clearly show the broadening expected from pile-up.

A simple simulation was performed to reproduce these effects. This entailed using Poisson statistics to calculate the probability that, for a given intensity, one or more pulses would pile up within the relevant time interval. The pile-up pulses were distributed randomly relative to the trigger-time, and summed using the known pulse shape[20]. Subsequently, the resulting voltage response as a function of time, $V(t)$, was calculated. Using the resolution measured at lowest intensities, the values obtained for $V(t)$ were smeared out to account for the calorimeter sampling resolution. The baseline-subtracted signals were then calculated, V(peak time) - V(base time), yielding the energy response and resolution of the calorimeter. This simulated resolution is also shown as a function of rate in Fig. 24, and agrees well with the experimental results. This suggests that the observed degradation of resolution at high rates is consistent with the effects expected from pile-up.

The occupancy rate at the Tevatron may be crudely estimated assuming an average multiplicity of 50 particles per interaction, an inelastic cross section of 50 mb, and that a hadronic shower deposits significant energy over roughly 10 towers (each with $\Delta\eta = \Delta\phi = 0.1$). The rate of particles entering this 10 tower region is 25 kHz at a luminosity of $5 \times 10^{30}\mathrm{cm}^{-2}\mathrm{s}^{-1}$, rising to 500 kHz at a luminosity of $10^{32}\mathrm{cm}^{-2}\mathrm{s}^{-1}$. Of course, the average energy of these particles is much less than 150 GeV, but we may use Fig. 24 as a guide; it shows that pile-up should not broaden the resolution significantly at the lower luminosity, which is what is foreseen for the 1992 collider run. However, if the Tevatron luminosity is upgraded significantly, pile-up could become a problem using the present calorimeter readout. There is therefore a plan to replace components in the electronics in order to reduce the intrinsic noise and shorten the sampling time, so that the calorimeter performance is not degraded at higher luminosities.

9 Electron-pion discrimination

The spatial development of electromagnetic and hadronic showers is quite different and so the shower shapes can be exploited to differentiate between electrons and hadrons. To obtain the best discrimination against hadrons, and to maximize the efficiency of electron-finding, one should use both longitudinal and transverse shower shape and also take account of correlations between energies in the various calorimeter cells.

We have used an H-matrix technique[21], which satisfies the above objectives, to carry out electron-finding and hadron rejection. In this technique, a "training" sample of Monte Carlo-generated electron showers is used to compute the mean energy $< E_i >$ deposited in each detector cell i, together with its correlation coefficient C_{ij} with the energy E_j deposited in every other cell j:

$$C_{ij} = < (E_i - < E_i >)(E_j - < E_j >) > . \qquad (9)$$

We then define the H-matrix by:

$$H_{ij} = C_{ij}^{-1}. \qquad (10)$$

For each event, an effective χ^2 is calculated from:

$$\chi^2 = \sum_{i,j}(E_i - < E_i >)H_{ij}(E_j - < E_j >). \tag{11}$$

A cut is then placed on the χ^2 to define an electron and to separate electrons from hadrons.

Electron-hadron separation is performed in two stages. First, a cut on the ratio of energy in the hadronic to electromagnetic calorimeter sections, *HAD/EM*, is used as an initial electron selection. We then use an H-matrix, "trained" on electrons, with 72×72 elements, including the energies in all cells within a $\Delta\eta \times \Delta\phi = 0.3 \times 0.3$ transverse area centered on the shower. These steps therefore take account of transverse as well as longitudinal shape and correlations, and can also be used to predict the particle entry position in the calorimeter. Our approach is to parameterize the elements of the H-matrix as a function of reconstructed energy (5 to 100 GeV) and pseudorapidity, and then use the parametrization to create an H-matrix appropriate for each shower energy in the data.

This technique was applied to samples of test beam electrons. The χ^2 cuts were chosen to obtain an electron efficiency of 95%. The pion rejection factor was then determined by applying the same cuts to pion test beam data. The rejection factors are shown in Fig. 25 as a function of pion momentum, for the case of cutting only on *HAD/EM*< 0.02, and for the case of a cut on *HAD/EM*< 0.04 followed by the H-matrix. Both of these give an electron efficiency of about 95%. The results at high momenta (≥ 100 GeV/c) are given as lower limits at 90% confidence level due to the limited statistics of the test beam pion data sample ($\sim 6500 - 3200$ events/momentum setting). The covariance matrix method significantly improves the pion rejection over the *HAD/EM* cut. The π rejection factor is $\sim 900 - 3000$ for particles in the momentum range between 50 and 150 GeV/c.

10 Muon response

Using the small fraction of muons (originating from pion decay) in the pion beam, the ECEM and ECIH calorimeter module response to muons was studied under the same experimental conditions as used for electrons and pions. The arrangement of the calorimeter modules and the muon beam counters is shown in Fig.5. Counters which were placed behind the calorimeter, labelled S_2 and S_3 in Fig.5, were used in tagging these muons. The total thickness of the calorimeter modules was 9.42 interaction lengths, which was followed by 17.9 interaction lengths of steel to stop any punchthrough hadrons; this material sets a passing muon momentum threshold of 4.8 GeV/c. Muon data were taken using a coincidence trigger $S_1 \cdot S_2 \cdot S_3$; pedestal triggers were interspersed randomly with the muon triggers during the spill. Data were taken at four different momenta: 15, 50, 100 and 150 GeV/c.

In contrast with electrons or pions, the muons deposit only a very small fraction of their energy in the calorimeter, and only a small fraction of that (the sampling fraction) is in the active medium and thus observable. A 15 GeV/c muon, for example, deposits about 2% of its energy in the electromagnetic section of the ECEM and only about 8% of that is in the sensitive medium. Hence, the observed signal is much smaller for muons than for electrons or pions. Therefore noise is particularly significant for the muon signal. To minimize noise, the analysis of muon data was performed slightly differently from that of the pion and electron data. First, pedestals interspersed between the data events were used to calculate the mean and the standard deviation of the pedestal value of each cell for each run; these values were then used in the pedestal subtraction and in the zero suppression when analyzing the data. Second, only the cells adjacent to the projected track (obtained by extrapolating the beam track using the PWC information) were used in obtaining the signal. It was found that four projective towers (two nearest ϕ and two nearest η), were sufficient to collect the muon signal at $\eta = 2.3$ where the data were taken.

Two properties of the calorimeter modules were studied by using muon data, the uniformity in depth and the "μ/e" ratio for ECEM. It has been known both experimentally[22] and theoretically[23] that, especially at high energies, the energy loss of a muon is energy and material dependent. This is due to the fact that at higher energies additional sources of muon energy loss, e^+e^- pair production, bremsstrahlung and nuclear interaction, become important. The energy dependence of energy loss for relativistic muons is significantly different in passive (high Z) and active (low Z) layers in a sampling calorimeter[24]. As a result, the observed signal becomes more complicated, and a more careful treatment is required for muons than just regarding them as minimum ionizing particles (MIPs) traversing bulk material. Taking these complications into account, it has been suggested[14] that it is preferable to measure "μ/e" ratios at a well-defined energy or to convert the measured "μ/e" ratio to "*MIP/e*" ratio, in order to make comparison with other data meaningful.

10.1 Uniformity in depth

At low energies, where radiative processes are not significant, one could use the muon signal to study the uniformity of the calorimeter modules. If it is assumed that the energy of the δ-electrons is deposited locally in each argon layer, then one would expect the observed signal per unit thickness of active medium to be the same anywhere in the calorimeter, regardless of the number of active/passive layers and their thicknesses. Using this assumption, we have attempted to study the uniformity in depth by comparing the muon signal on individual layers of ECEM and ECIH modules, using the data at the lowest available momentum (15 GeV/c).

The pulse height distribution measured in several of the ECEM and ECIH layers, with their pedestal distributions, are shown in Fig.26 (a),(b),(c) and (d). The data points are fitted with the Moyal function [25],[26] (an approximate analytic expression for the Landau distribution), convoluted with a Gaussian resolution function. The most probable values obtained from the fit are given in the figure. It is the mean value of the pulse height, not the most probable value, that is proportional to the thickness of the medium traversed by the muon[25]. The mean pulse heights, as calculated from the fit, per unit thickness of the argon gap for individual layers are shown in Fig.27. The result shows the expected uniformity of the calorimeter.

10.2 "μ/e" ratio

As discussed earlier, the muon response is expected to be energy dependent. This can be seen in Fig.28 which shows the normalized pulse height distributions from muons of four different momenta (15, 50, 100 and 150 GeV/c) in the ECEM, together with a fit to the function described above. Both the mean and the most probable value (both obtained from the fit), shown in Fig.29, increase with energy, the latter to a lesser degree, as expected [24]. The spectrum becomes broader and more asymmetrical at higher energies owing to the contributions from radiative processes.

The above results clearly indicate that the signal in the calorimeter for a muon is always larger than that of a MIP. By comparing the observed signal with Monte Carlo results (using GEANT), we have estimated the MIP signal as follows. First, the Monte Carlo results were obtained for muons traversing the same position in the calorimeter with same energies as in the data. Then, the most probable value (in MeV) of the MC spectrum was obtained by fitting the Moyal function. The Monte Carlo results, converted to ADC counts using a constant factor for all energies, agree very well with the data as shown in Fig.29. These Monte Carlo points were also used to determine the ratio of muon pulse height to MIP dE/dx pulse height at each energy. Then the pulse height for a MIP in our data was extracted by reducing the measured muon pulse height according to the above ratio. The result is included in Fig.29 and is independent of energy, as expected.

In order to compare the electromagnetic-calorimeter response to muons with the response to electrons, we consider the ratio,

$$\frac{\mu}{e} = \frac{PH_\mu / E_\mu}{PH_e / E_e} \tag{12}$$

where PH_μ and PH_e are the measured pulse heights for muons and electrons respectively, E_e is the electron beam energy and E_μ is the total energy loss by a muon traversing the ECEM. All quantities except E_μ are measured experimentally. If one assumes that muons behaves as MIPs then E_μ can be calculated using the known[27] dE/dx values. The "μ/e" ratio obtained under such assumption is shown in Fig.30. The energy dependence of the "μ/e" is due to the energy dependence of PH_μ, which becomes smaller if the most probable value is used for PH_μ. By using the corrected PH for MIPs (as in Fig. 29) we obtained the "*MIP/e*" ratio which is energy independent as it should be.

It should be pointed out that to estimate the pulse height for MIPs from the experimental data one needs a reliable Monte Carlo simulation. Our study indicates that the best way to obtain an approximate value of the "*MIP/e*" ratio without such a simulation is to use the most probable value of the measured muon signal at the lowest possible energy. For the DØ ECEM the best estimate of the "*MIP/e*" ratio is 1.41±0.05.

Similar ratios have been observed in sampling calorimeters in other experiments. A detailed comparison of the data with Monte Carlo results [14] has shown that this behavior is due to the way in which low energy photons, which are abundantly produced in the electromagnetic shower development, interact with matter. Because of the strong Z-dependence of the photoelectric effect ($\propto Z^5$), most of these photons will transfer their energies to electrons in the high Z absorber rather than the low Z sensitive medium. Therefore the observed fraction of the energy deposited by these low energy photons is much smaller than would be expected from sampling fractions based on the energy loss for MIPs. This causes "*MIP/e*"> 1, which is an important factor in making the calorimeter response to electromagnetic and hadronic showers equal.

It may be noted that the ECEM calorimeter is just behind a cryostat wall. This acts as an integral part of the calorimeter as it plays a part in the development of electromagnetic showers. If we include the cryostat, the MIP energy deposited therein must be counted in the calculation of the expected energy loss, lowering the "*MIP/e*" ratio of the cryostat-plus-ECEM calorimeter. In this case the measured value becomes 1.22±0.05.

11 Conclusions

Three uranium-liquid argon calorimeter modules constructed for the DØ detector at the Fermilab Tevatron collider have been tested with beams of electrons, pions and muons between 10 and 150 GeV/c. The performance of the system, including the cryogenics, high voltage, calibration, readout and argon purity monitoring appears excellent. Good energy resolution has been obtained for electrons and hadrons; and the linearity, compensation and electron-hadron discrimination power of the detectors has been well demonstrated. The results agree well with predictions of a detailed Monte Carlo simulation.

Acknowledgments

We are grateful for the support from the Accelerator and Research Divisions at Fermilab. We thank K. Holly, D. Kewley and S. Libonate for their help with these tests. This work was funded by the United States Department of Energy and the National Science Foundation.

References

1. S. H. Aronson *et al.*, Nucl. Instr. & Meth. A **269** (1988) 492.
2. M. Abolins *et al.*, Nucl. Instr. & Meth. A **280** (1989) 36.
3. H. Aihara, et al., "The Design, Construction, and Performance of the D0 End Calorimeter Electromagnetic Module", Lawrence Berkeley Laboratory Report LBL-31378 (to be published in Nucl. Instr. & Meth.).
4. R. Brun et al., CERN-DD/EE/84-1, May 1986.

5. H. B. Prosper, "Data Driven Geometry for GEANT", Proc. of the International Conference on Calorimetry in High Energy Physics, Fermilab (1990) p 546.
6. R.D. Schamberger, Nucl. Phys. B (Proc. Suppl.) **23A** (1991) 191.
7. V. Radeka, S. Rescia, Nucl. Instr. & Meth. **A265** (1988) 228.
8. M. Demarteau, "D0 Calorimeter Electronics Performance", Proc. of the International Conference on Calorimetry in High Energy Physics, Fermilab (1990) p 91.
9. P. Franzini, D0 note 750, Fermilab, unpublished
10. J. Kourlas, J. Sculli, D0 note 936, Fermilab, unpublished
    J. Kourlas, D0 note 970, Fermilab, unpublished
11. G.C. Blazey, et al., "Monitoring Liquid Argon Purity at D0", Proc. of the International Conference on Calorimetry in High Energy Physics, Fermilab (1990) p 101.
12. W.Hoffmann. et al., Nucl. Inst. and Meth. **135** (1976) 151.
13. G.A. Akopdjanov *et al.*, Nucl. Inst. & Meth **140** (1977) 441, A. DeAngelis and F. Mazzone, Nucl. Inst. & Meth **A 287** (1990) 397.
14. R. Wigmans, Nucl. Inst. & Meth. **A 259** (1987) 389; *ibid.* **A 265** (1988) 273.
15. J. Womersley, Nucl. Inst. & Meth **A 289** (1990) 475.
16. H. Fesefeldt, RWTH Aachen report RWTH/PITHA 85/02.
17. K. Hänssgen and J. Ranft, Comp. Phys. Comm. **39** (1986) 37; *ibid.* **39** (1986) 53.
18. R.K. Bock *et al.*, Nucl. Instr. and Meth. **186** (1981) 533-539 .
19. M.De Palma *et al.*, Nucl. Instr. and Meth. **219** (1984) 87-96 .
20. P. Franzini D0 Note 77, Fermilab, unpublished.
21. R. Engelmann *et al.*, Nucl. Instr. & Meth. **216** (1983) 45.
22. T. Åkesson *et al.*, Nucl. Instr. & Meth. **A262** (1987) 243.
23. W. Lohmann, R. Kopp and R. Voss, Energy loss of muons in the energy range 1-10000 GeV; CERN Report CERN 85-03 (1985)

24. B. Anders, U. Behrens and H. Brückmann, Nucl. Instr. & Meth. **A270** (1988) 140.

25. E. Bernardi, On the Optimization of the energy resolution of hadronic calorimeters, Dissertation, Universität Hamburg, Hamburg (1987)

26. J. E. Moyal, Theory of ionization fluctuations, Phil. Mag. **46** (1955) 263.

27. Review of Particle Properties, Phys. Lett. **B 170** (1986) 1.

Figure 1: Isometric cutaway drawing of the calorimeters of the D0 detector.

Figure 2: Cross section through the basic sampling cell of the ECEM and ECIH calorimeters, showing uranium plates, liquid argon gaps and a multi-layer signal board.

Figure 3: Isometric view of an ECEM calorimeter module.

Figure 4: Schematic drawing of the Neutrino West test beam at Fermilab showing the beam line elements.

Figure 5: Arrangement of calorimeter modules within the cryostat.

Figure 6: Widths of pedestals taken in ×8 mode as a function of detector cell capacitance; the detector high voltage was off in (a), and at nominal voltage in (b).

Figure 7: Simulated distribution of pedestals, in ADC counts, for a central IH tower, including the effects of uranium decays convoluted with capacitative noise (points); superimposed is a measured pedestal distribution (solid line).

Figure 8: Schematic of the pulser input to the D0 calorimeter preamplifier.

Figure 9: Response of a single channel to different pulser amplitude settings. The pulser amplitude is in arbitrary units.

Figure 10: Normalized gain of a typical channel as a function of time (corrected for BLS and preamp temperature variations).

Figure 11: Calorimeter response to electrons, and the response of an argon β test cell, as a function of high voltage across the 2.3 mm gap (curves normalized at 3.0 kV).

Figure 12: *Energy spectra measured in the calorimeter for runs with electron* beams with momentum of 10, 25, 50, 75, 100, 125, and 150 GeV/c. 1000 events are used for each run.

Figure 13: Calorimeter linearity and energy resolution for electrons: (a) Fractional deviation of the mean reconstructed energy from the mean track momentum, as a function of beam momentum; (b) Fractional energy resolution as a function of beam momentum. The parameters of the fit are given in the text.

Figure 14: Position resolution obtained in the ECEM, as a function of energy, using the corrected center-of-gravity technique. Both the resolution at the tower edge, and the resolution integrated over the tower width at η=1.95 (where the pad size in EM3 is 2.6 cm) are shown.

Figure 15: The sum of the ECEM + ECIH response to 100 GeV/c pions, with EM1 $<$ 0.51 GeV, and without any cut on EM1 energy.

Figure 16: Deviations from a linear fit to the mean hadronic pulse height, as a function of beam momentum.

Figure 17: Pion resolution for ECEM+ECIH calorimeters, as a function of beam momentum, with and without the $EM1 < 0.51$ GeV cut. Also shown are Monte Carlo points for the case of $EM1 < 0.51$ GeV.

Figure 18: Hadronic energy response in the ECMH module, for 150 GeV/c pions, showing the low-energy tail due to interactions in upstream material.

Figure 19: Fractional hadronic and electromagnetic energy resolution as a function of beam momentum for the ECMH module.

Figure 20: (a) The electromagnetic to hadronic response ratio (e/π), as a function of beam momentum, for the sum of the ECEM and ECIH modules, using 15×15 towers around the beam and $EM1 < 1.2$ GeV; (b) e/π corrected for transverse shower leakage and $EM1$ cut.

Figure 21: Distributions of energy in the third ECEM layer and in the first ECIH layer for 100 GeV/c pion showers (solid line), and GEANT/GHEISHA Monte Carlo (dashed line) for comparison.

Figure 22: Mean energy deposited per interaction length for the calorimeter readout layers as a function of depth in the calorimeter. Pion showers are shown together with Monte Carlo and the shower parameterization.

Figure 23: Mean pulse height for 100 GeV/c pions as a function of pseudorapidity, for data and for the shower parameterization.

Figure 24: Fractional energy resolution as a function of beam intensity for 150 GeV/c pions, showing effects of pile-up as a function of the number of beam particles incident per second.

Figure 25: Pion rejection factors for 95% electron efficiency, as a function of pion momentum. The points shown are for a cut on the ratio of hadronic to electromagnetic energy $HAD/EM < 0.02$, and for $HAD/EM < 0.04$ used together with the H-matrix scheme. The upward arrows indicate points which are lower limits.

Figure 26: Pulse height and pedestal distributions in four calorimeter layers for 15 GeV/c muons.

Figure 27: Mean pulse height for 15 GeV/c muons, per unit argon thickness, as a function of calorimeter layer.

Figure 28: Muon pulse height spectrum in ECEM fitted with a Moyal/Gaussian convolution at 15, 50, 100 and 150 GeV/c; the most probable value (MPV) is shown.

Figure 29: The mean, the most probable value (MPV) for data and Monte Carlo, and the deduced MIP pulse height, as a function of momentum for muons in the ECEM (MC results converted to ADC counts.)

Figure 30: μ/e ratio as a function of energy. Shown are the ratios obtained using the mean, the most probable value and the MIP pulse height.

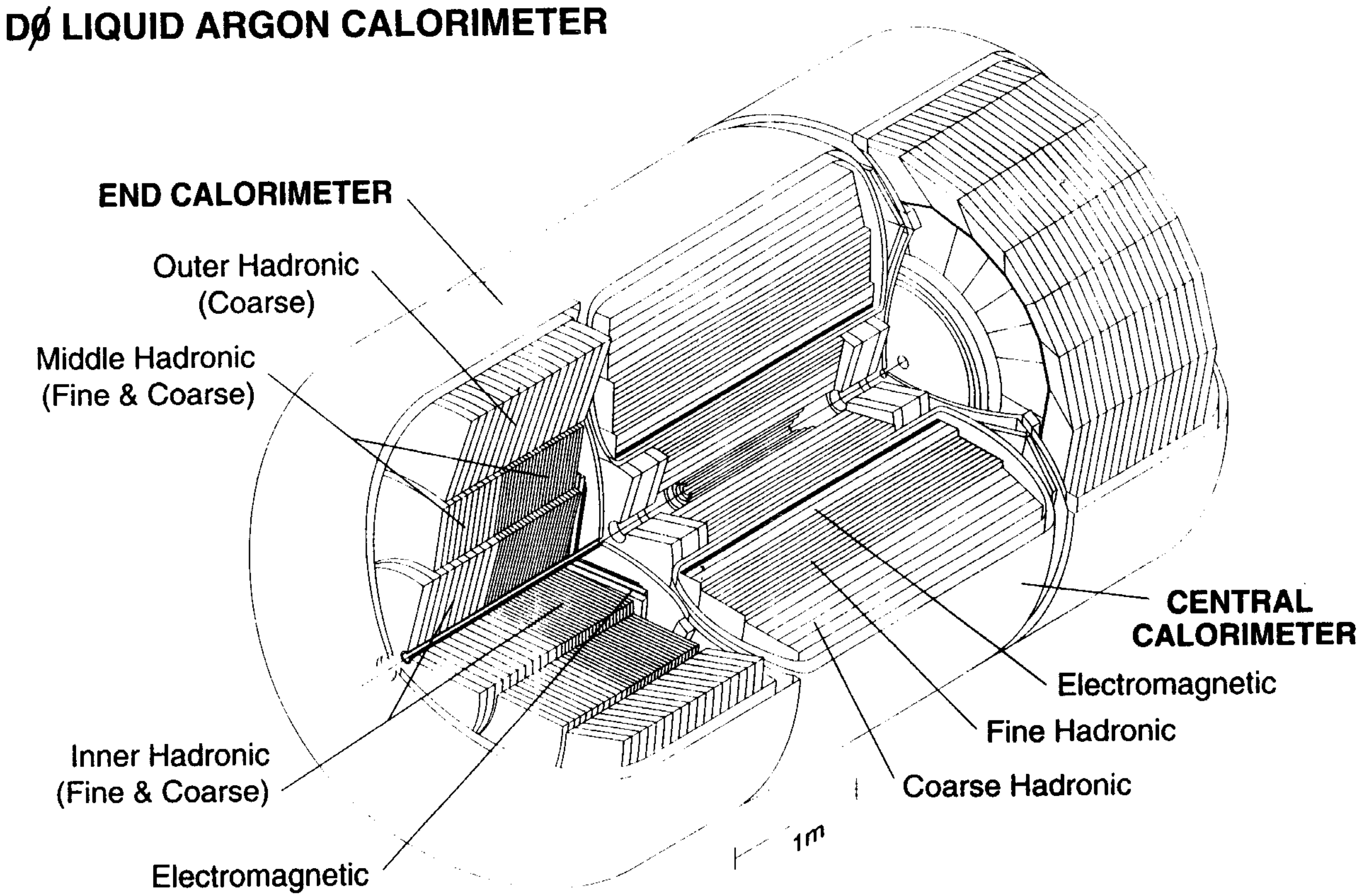
D0 LIQUID ARGON CALORIMETER
END CALORIMETER
Outer Hadronic (Coarse)
Middle Hadronic (Fine & Coarse)
Inner Hadronic (Fine & Coarse)
Electromagnetic
CENTRAL CALORIMETER
Electromagnetic
Fine Hadronic
Coarse Hadronic
1m

Figure 1

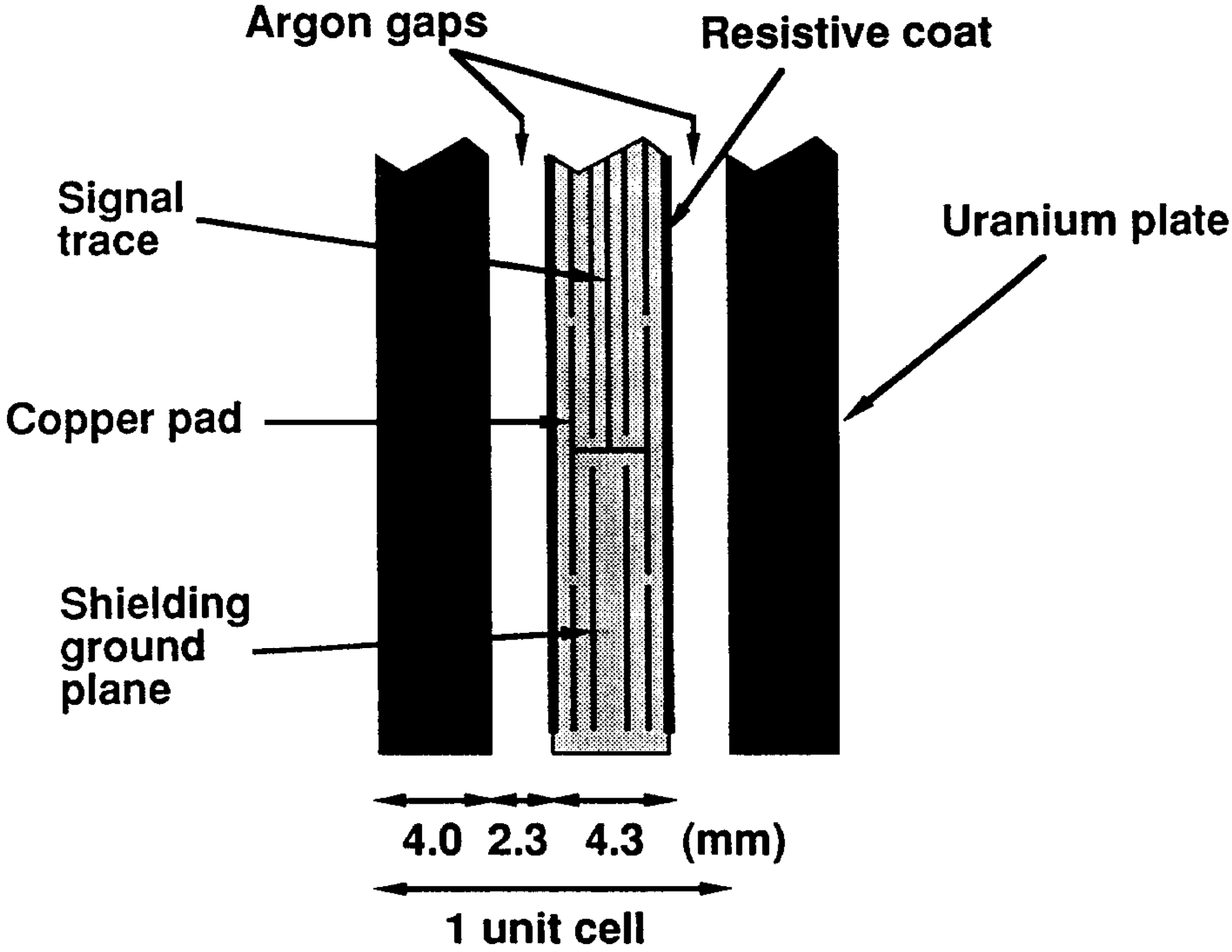
Argon gaps
Resistive coat
Signal trace
Uranium plate
Copper pad
Shielding ground plane
4.0
2.3
4.3
(mm)
1 unit cell

Figure 2

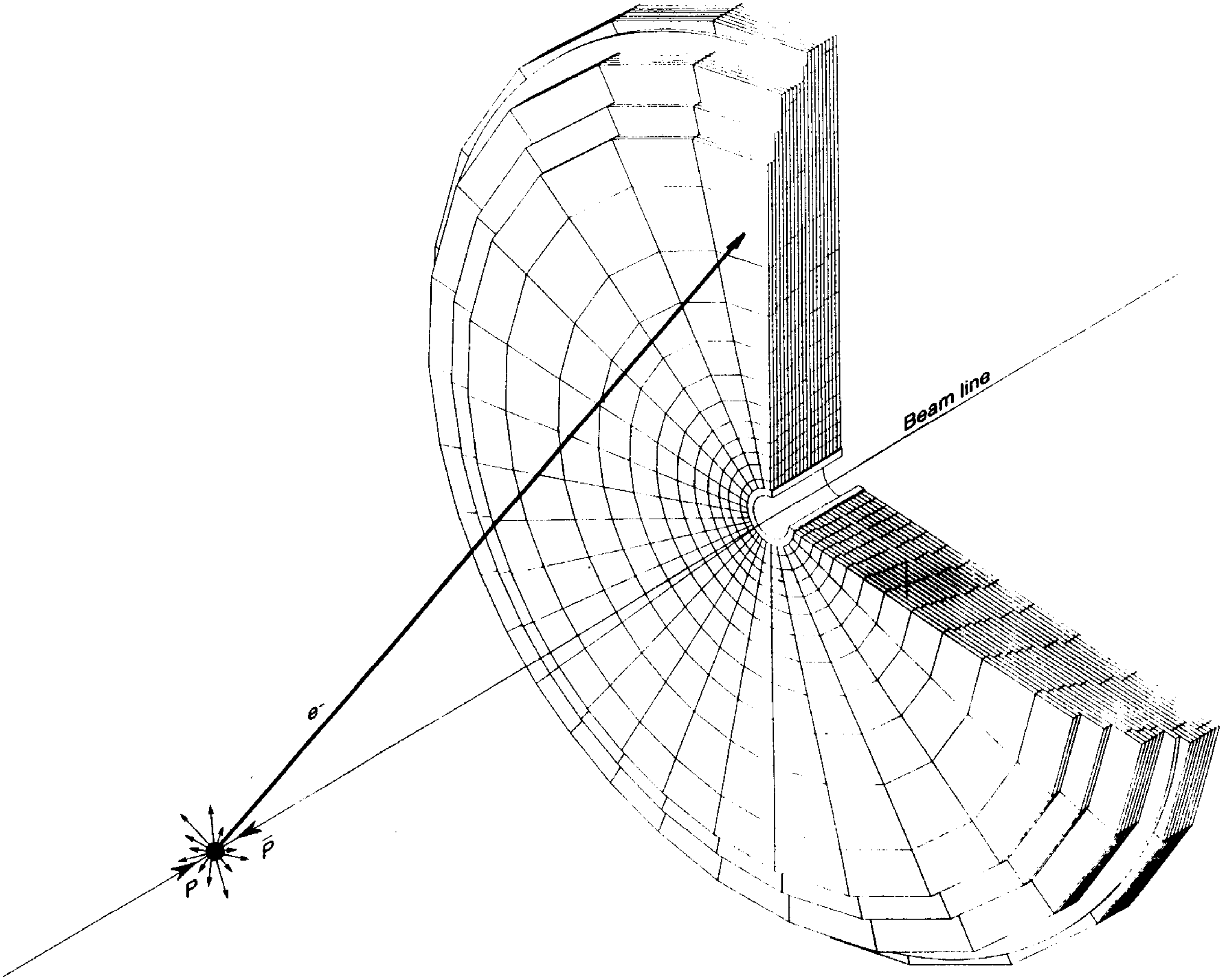

DØ END CALORIMETER ELECTROMAGNETIC MODULE

Figure 3

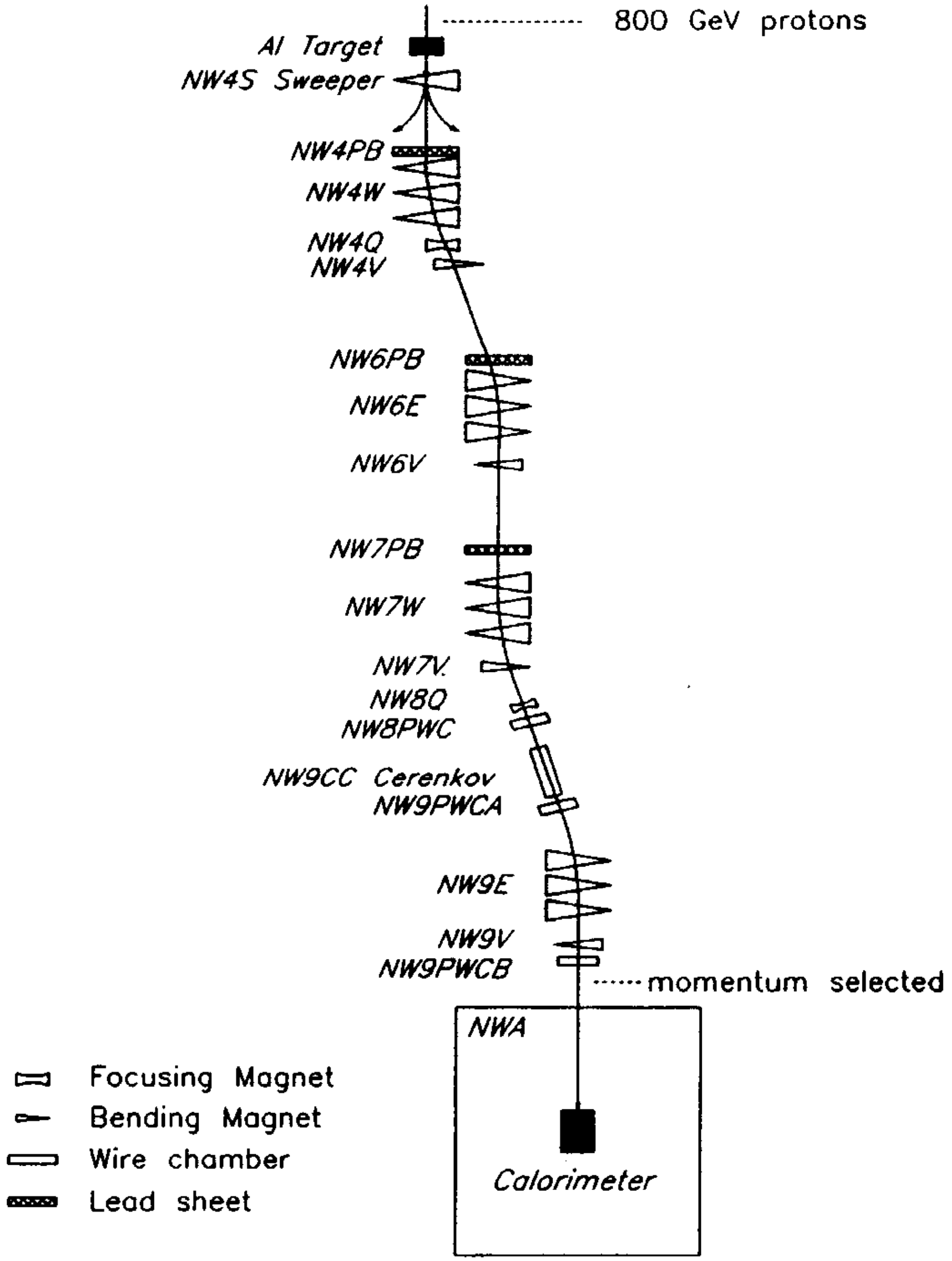
800 GeV protons
Al Target
NW4S Sweeper
NW4PB
NW4W
NW4Q
NW4V
NW6PB
NW6E
NW6V
NW7PB
NW7W
NW7V.
NW8Q
NW8PWC
NW9CC Cerenkov
NW9PWCA
NW9E
NW9V
NW9PWCB
momentum selected
NWA
Calorimeter
Focusing Magnet
Bending Magnet
Wire chamber
Lead sheet

Figure 4

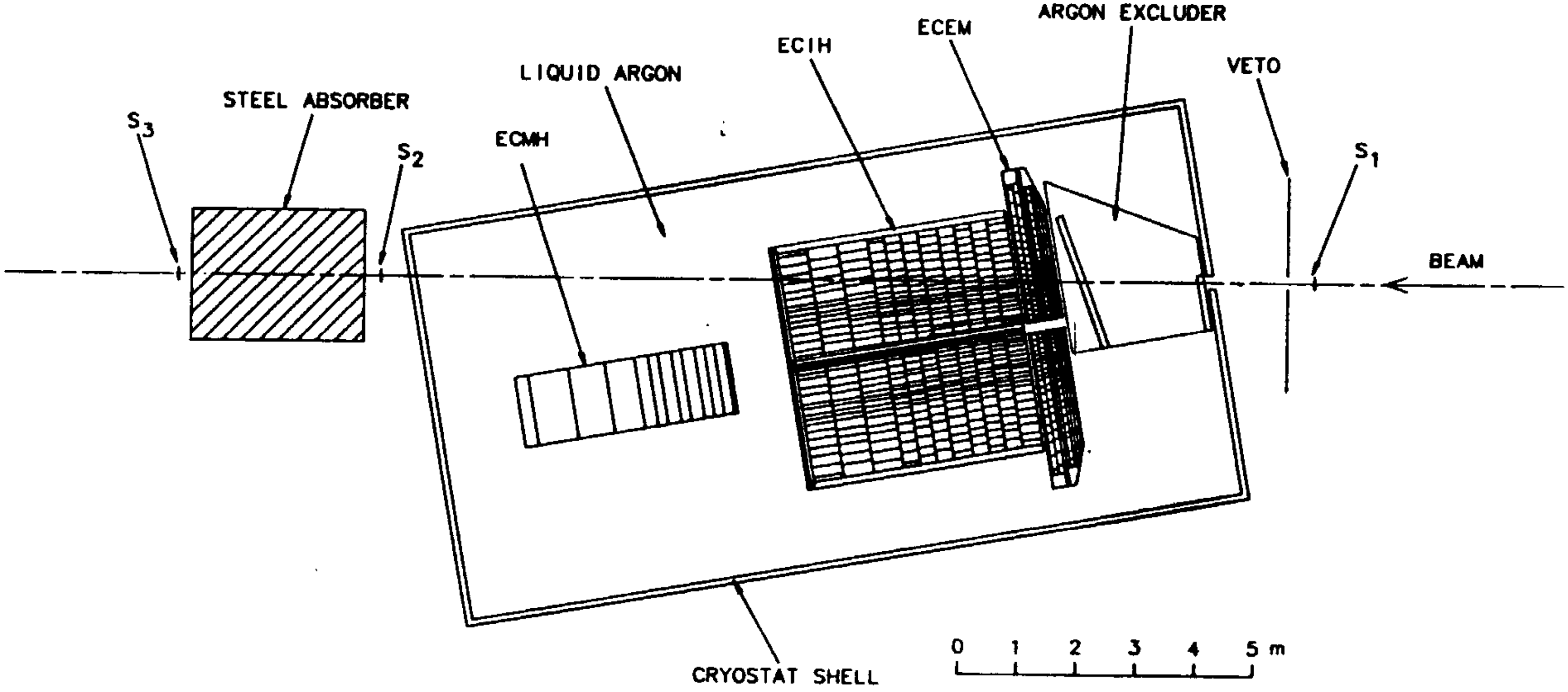
STEEL ABSORBER
S_3
S_2
ECMH
LIQUID ARGON
ECIH
ECEM
ARGON EXCLUDER
VETO
S_1
BEAM
CRYOSTAT SHELL
0 1 2 3 4 5 m

Figure 5

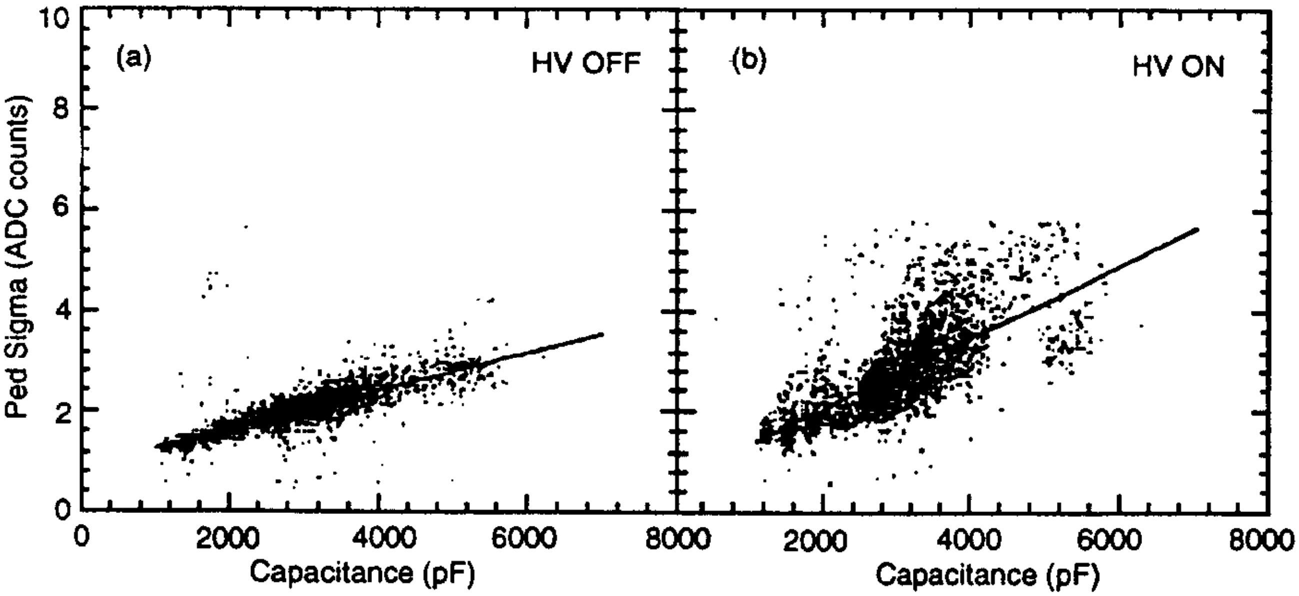
Ped Sigma (ADC counts)
10
8
6
4
2
0
(a)
HV OFF
(b)
HV ON
0
2000
4000
6000
8000
2000
4000
6000
8000
Capacitance (pF)
Capacitance (pF)

Figure 6

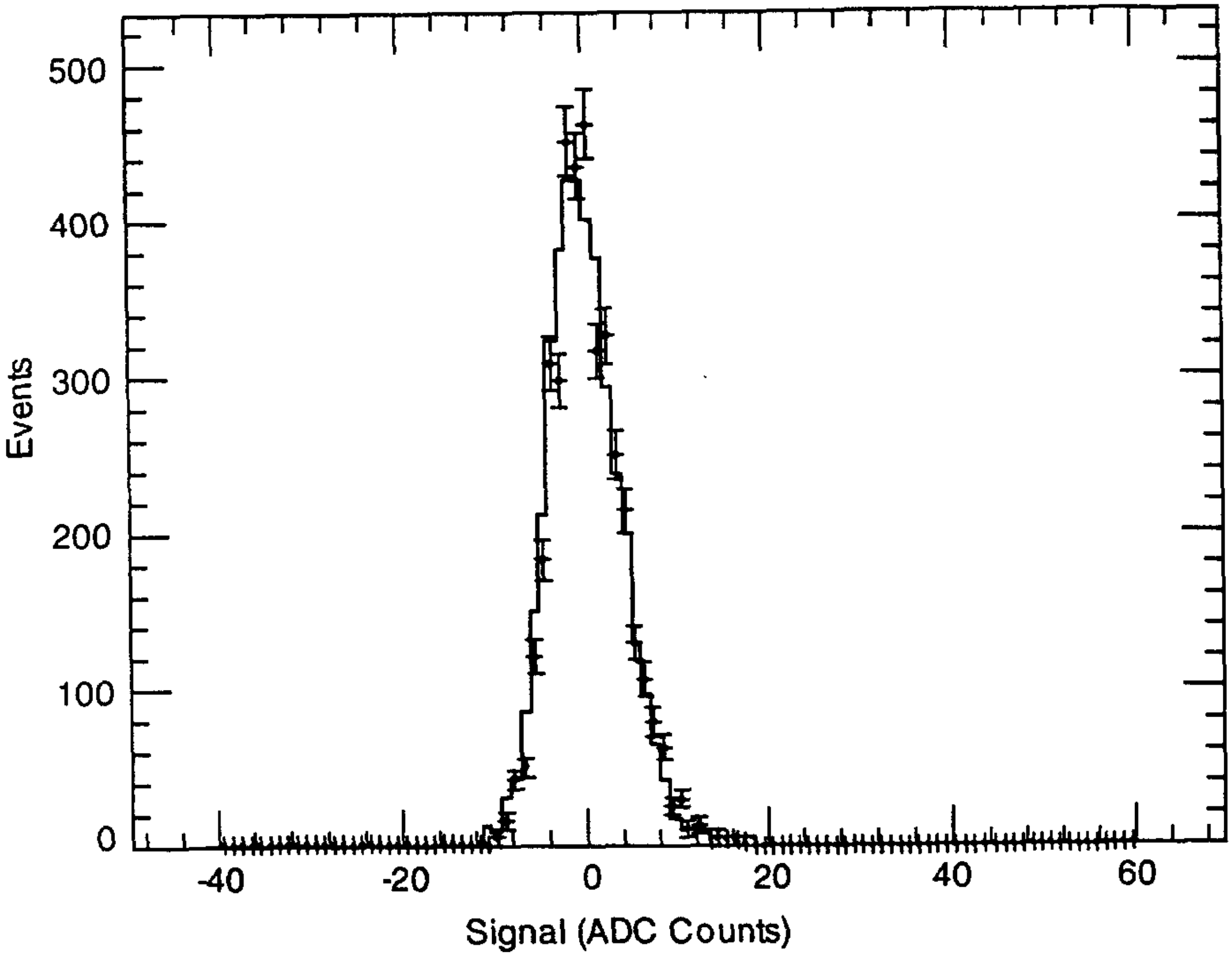

Figure 7

womersley s3 7lb

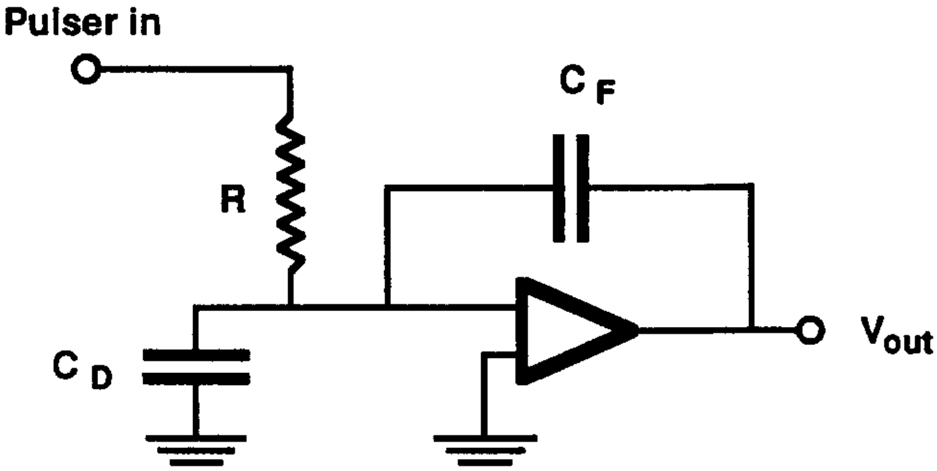

Figure 8

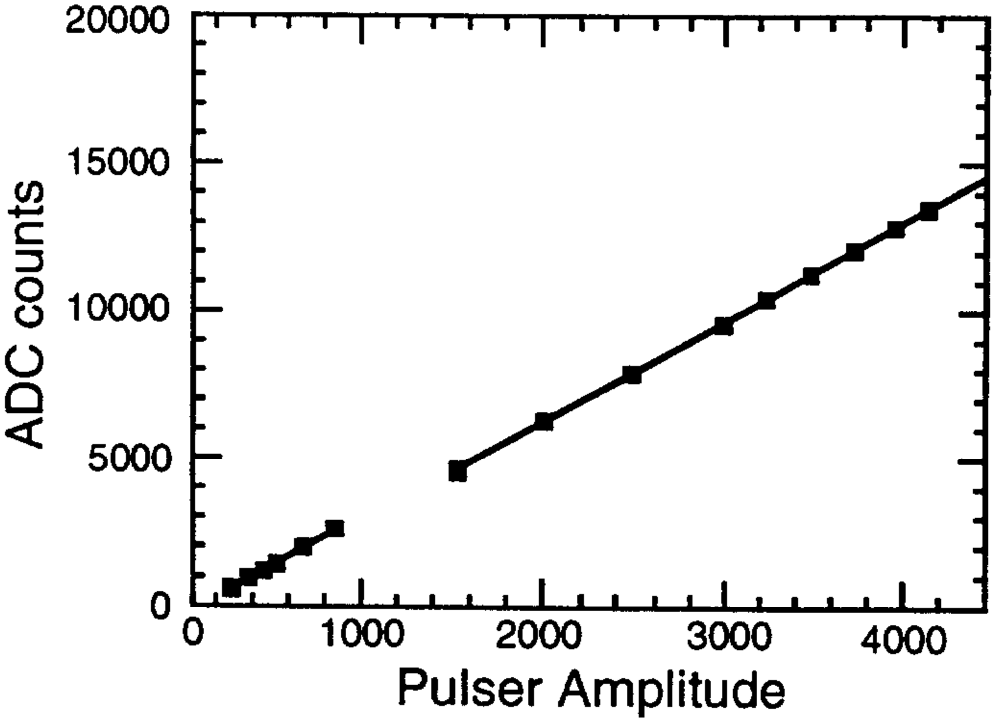
20000
15000
10000
5000
0
ADC counts
0
1000
2000
3000
4000
Pulser Amplitude

Figure 9

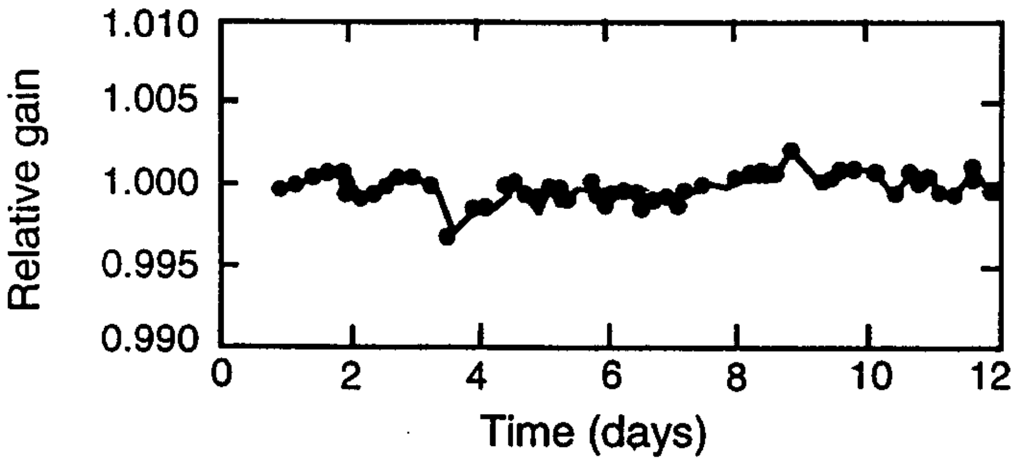

Figure 10

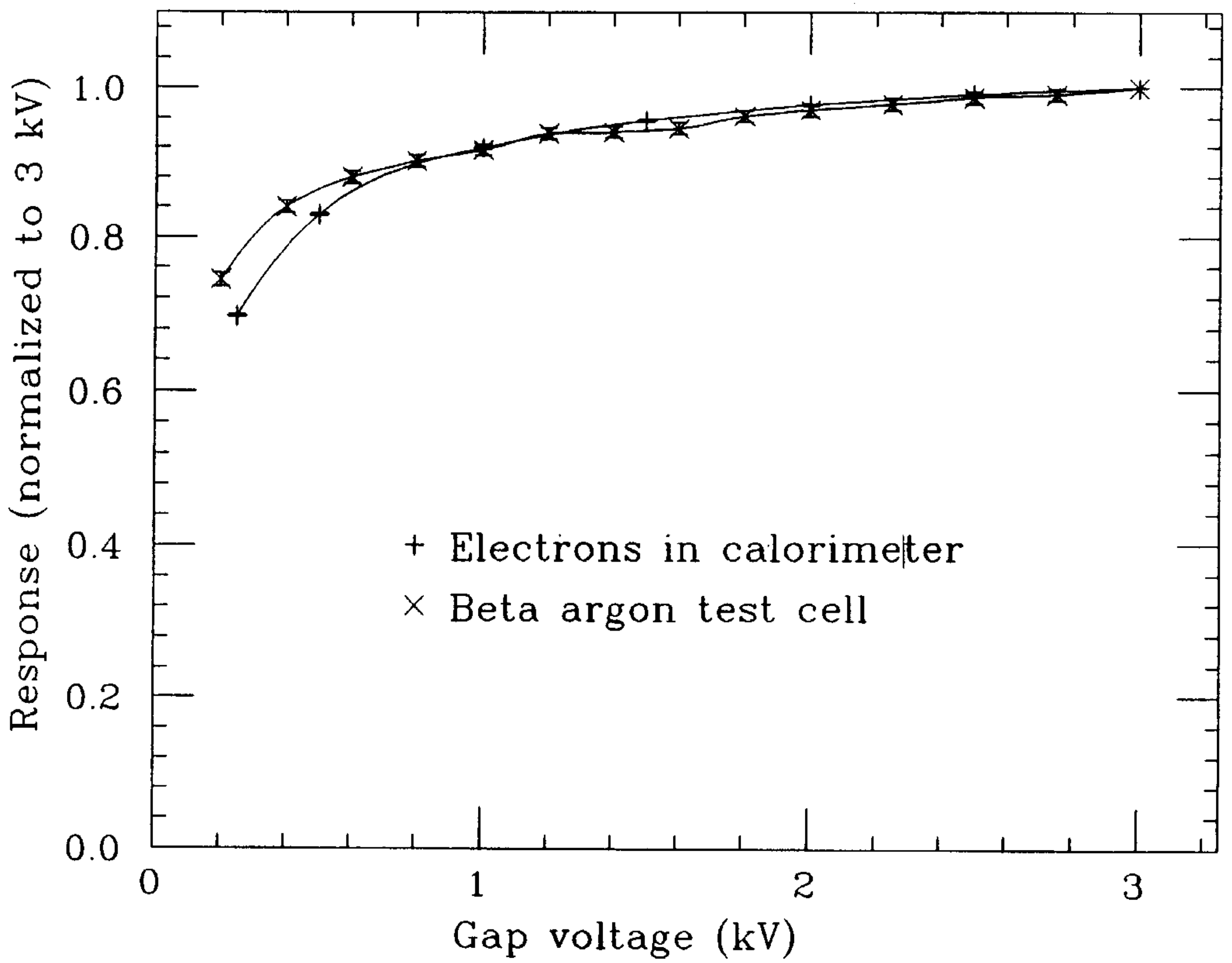
Response (normalized to 3 kV)
0.0
0.2
0.4
0.6
0.8
1.0
0
1
2
3
Gap voltage (kV)
+ Electrons in calorimeter
× Beta argon test cell

Figure 11

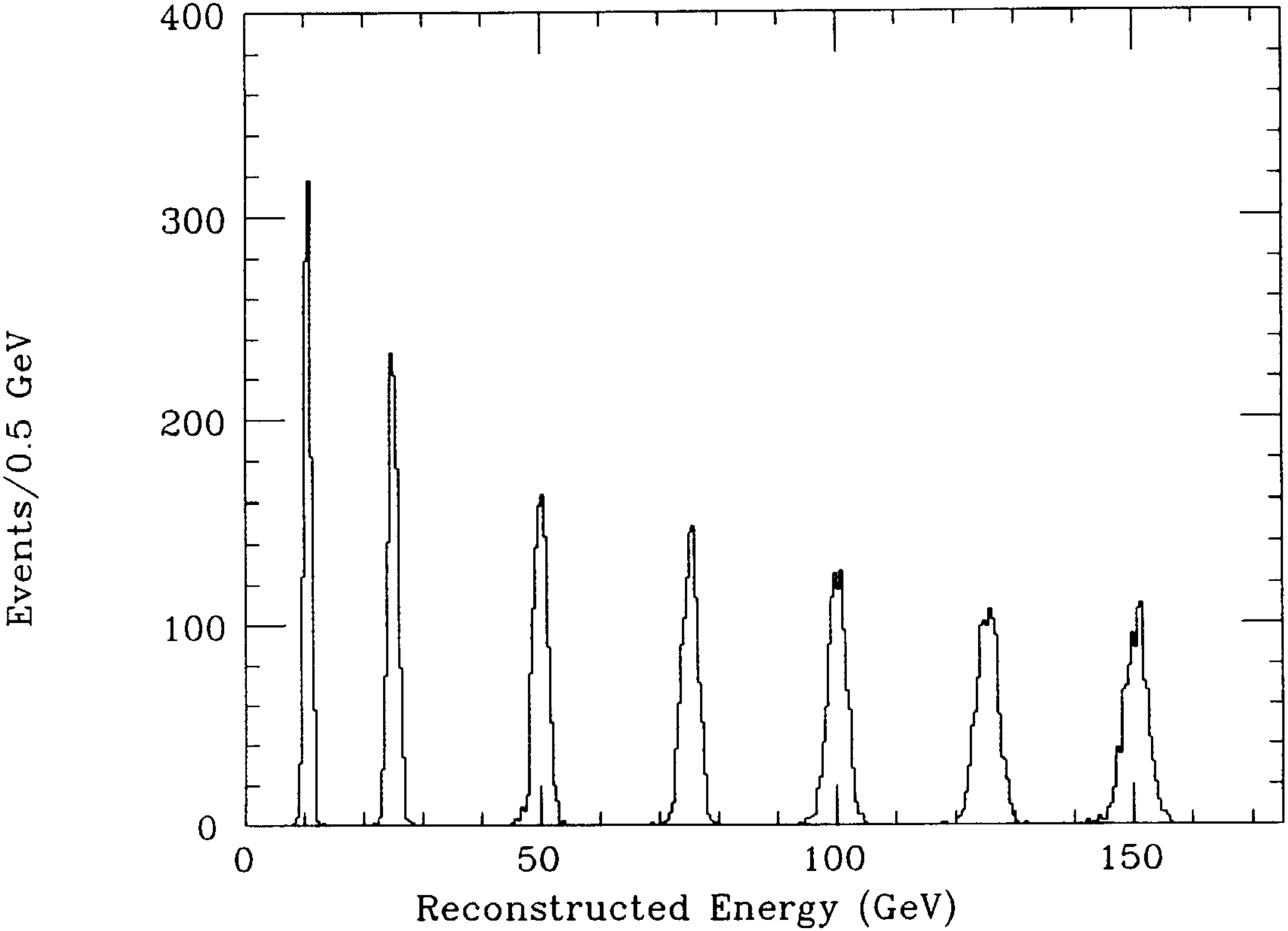
Events/0.5 GeV
0
100
200
300
400
0
50
100
150
Reconstructed Energy (GeV)

Figure 12

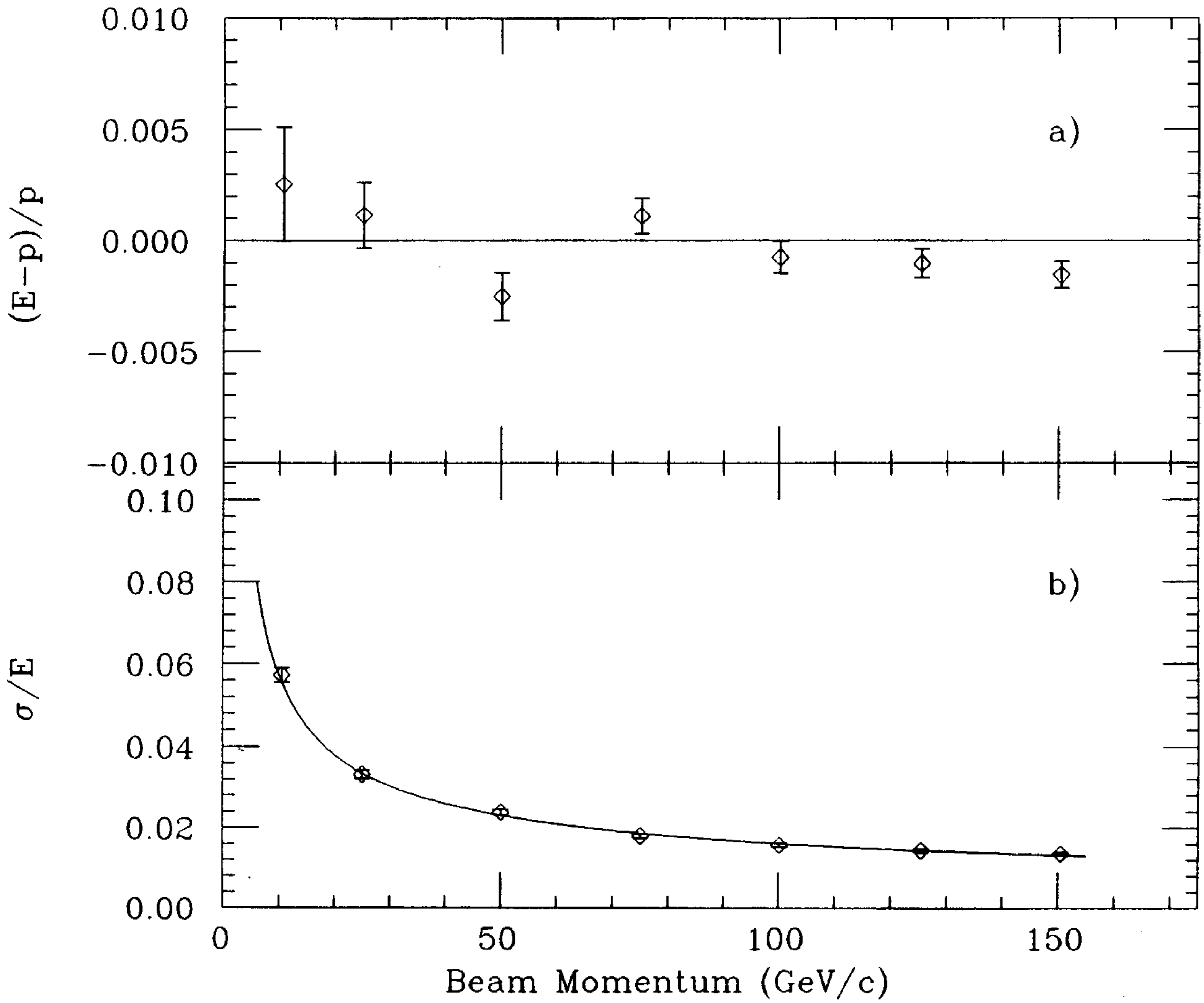
0.010
0.005
0.000
−0.005
−0.010
(E−p)/p
a)
0.10
0.08
0.06
0.04
0.02
0.00
σ/E
b)
0
50
100
150
Beam Momentum (GeV/c)

Figure 13

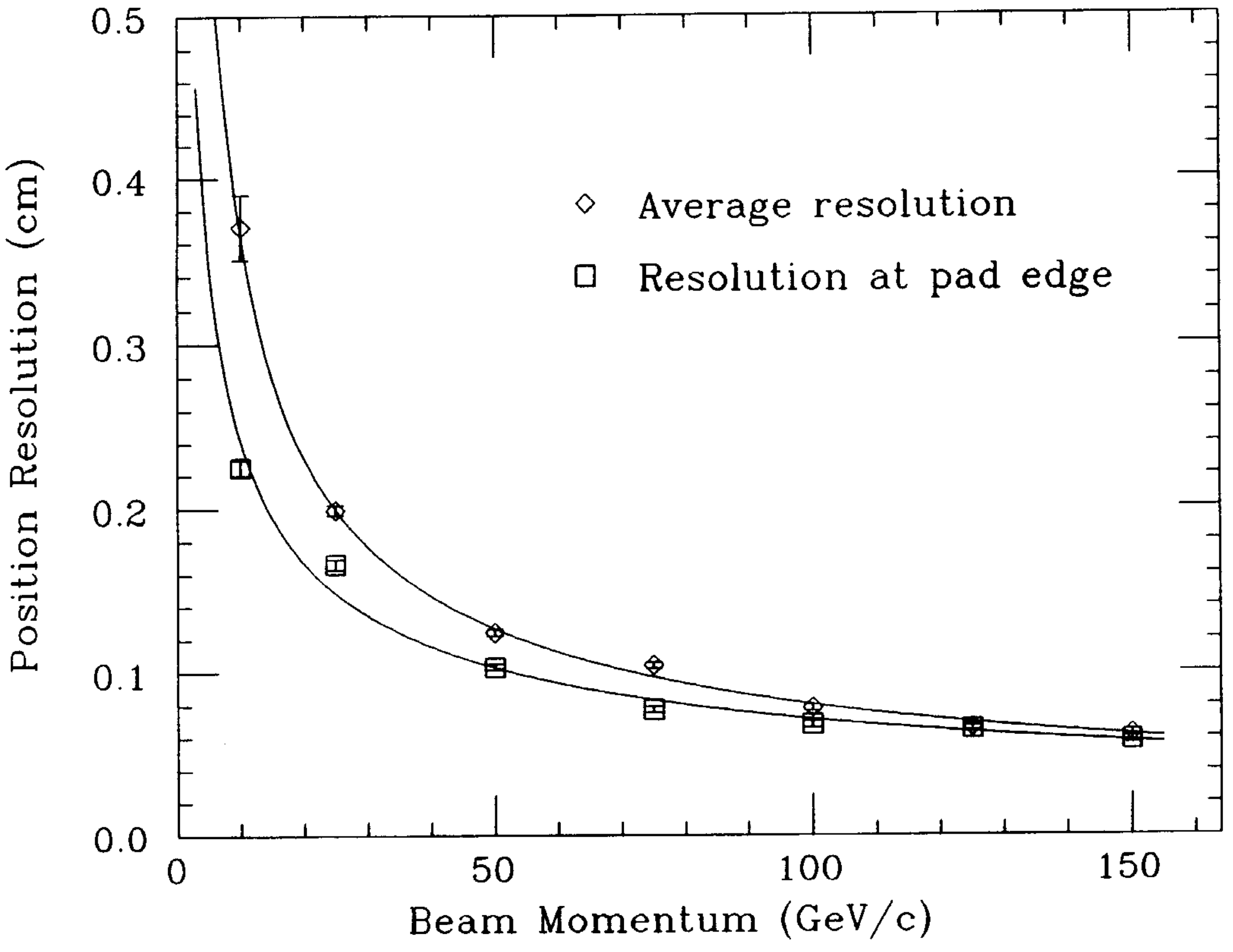
0.5
0.4
0.3
0.2
0.1
0.0
Position Resolution (cm)
0
50
100
150
Beam Momentum (GeV/c)
◇ Average resolution
□ Resolution at pad edge

Figure 14

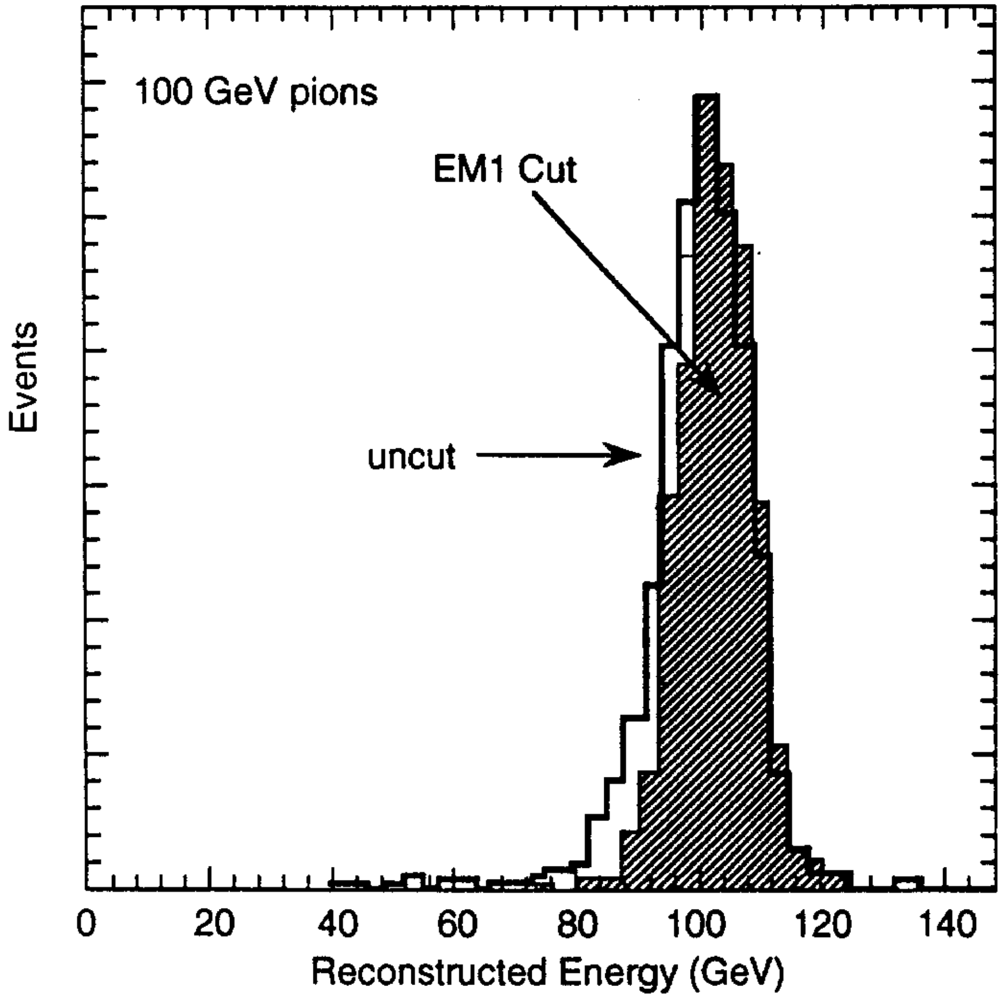
100 GeV pions
EM1 Cut
uncut
Events
0
20
40
60
80
100
120
140
Reconstructed Energy (GeV)

Figure 15

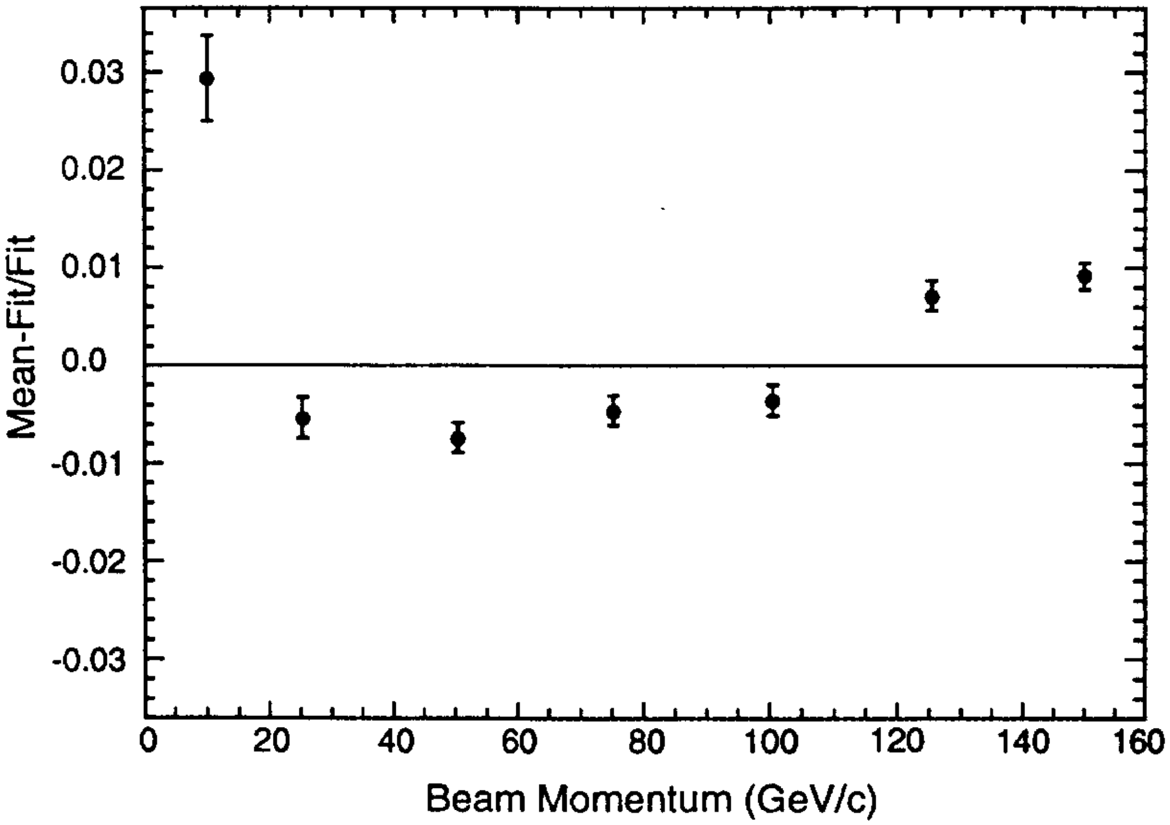
Mean-Fit/Fit
0.03
0.02
0.01
0.0
-0.01
-0.02
-0.03
0
20
40
60
80
100
120
140
160
Beam Momentum (GeV/c)

Figure 16

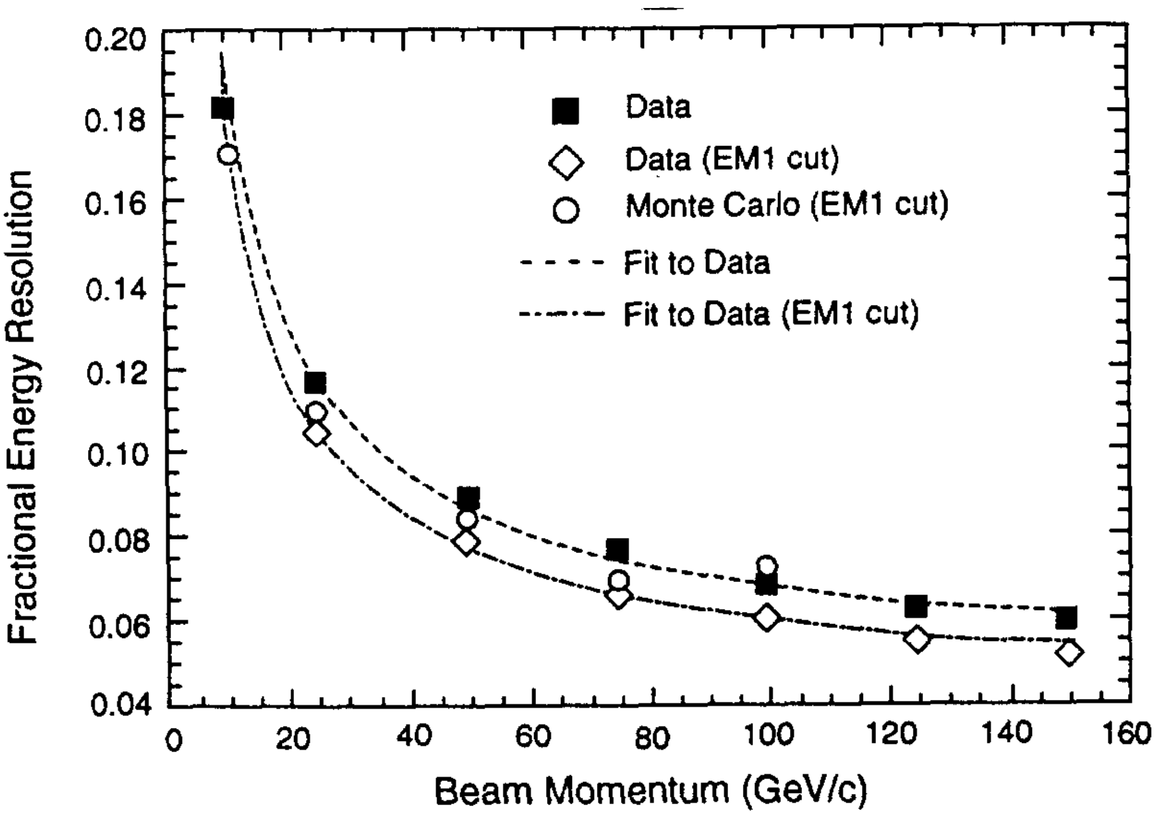

0.20
0.18
0.16
0.14
0.12
0.10
0.08
0.06
0.04
Fractional Energy Resolution
0
20
40
60
80
100
120
140
160
Beam Momentum (GeV/c)
■ Data
◇ Data (EM1 cut)
○ Monte Carlo (EM1 cut)
Fit to Data
Fit to Data (EM1 cut)

Figure 17

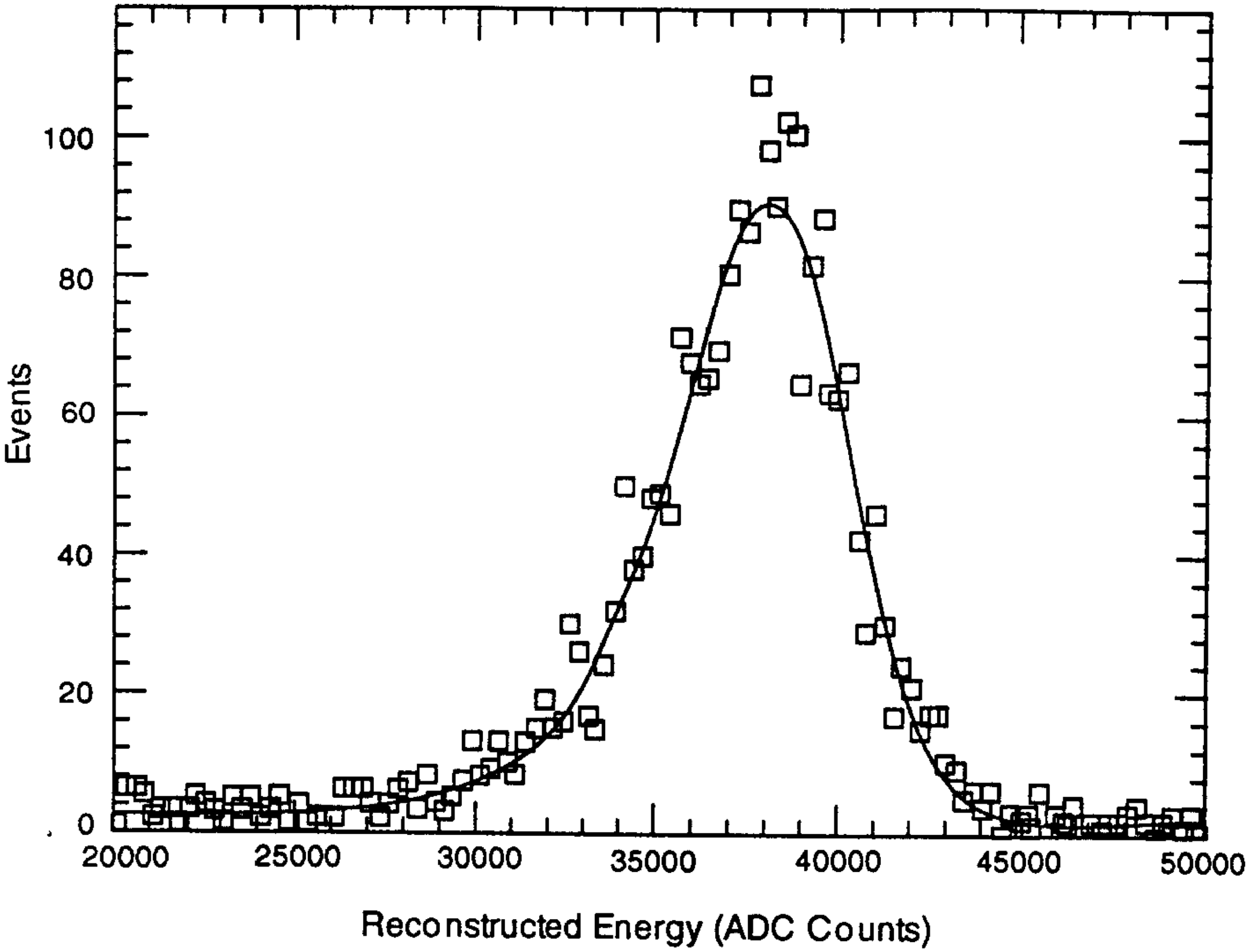
Events
0
20
40
60
80
100
20000
25000
30000
35000
40000
45000
50000
Reconstructed Energy (ADC Counts)

Figure 18

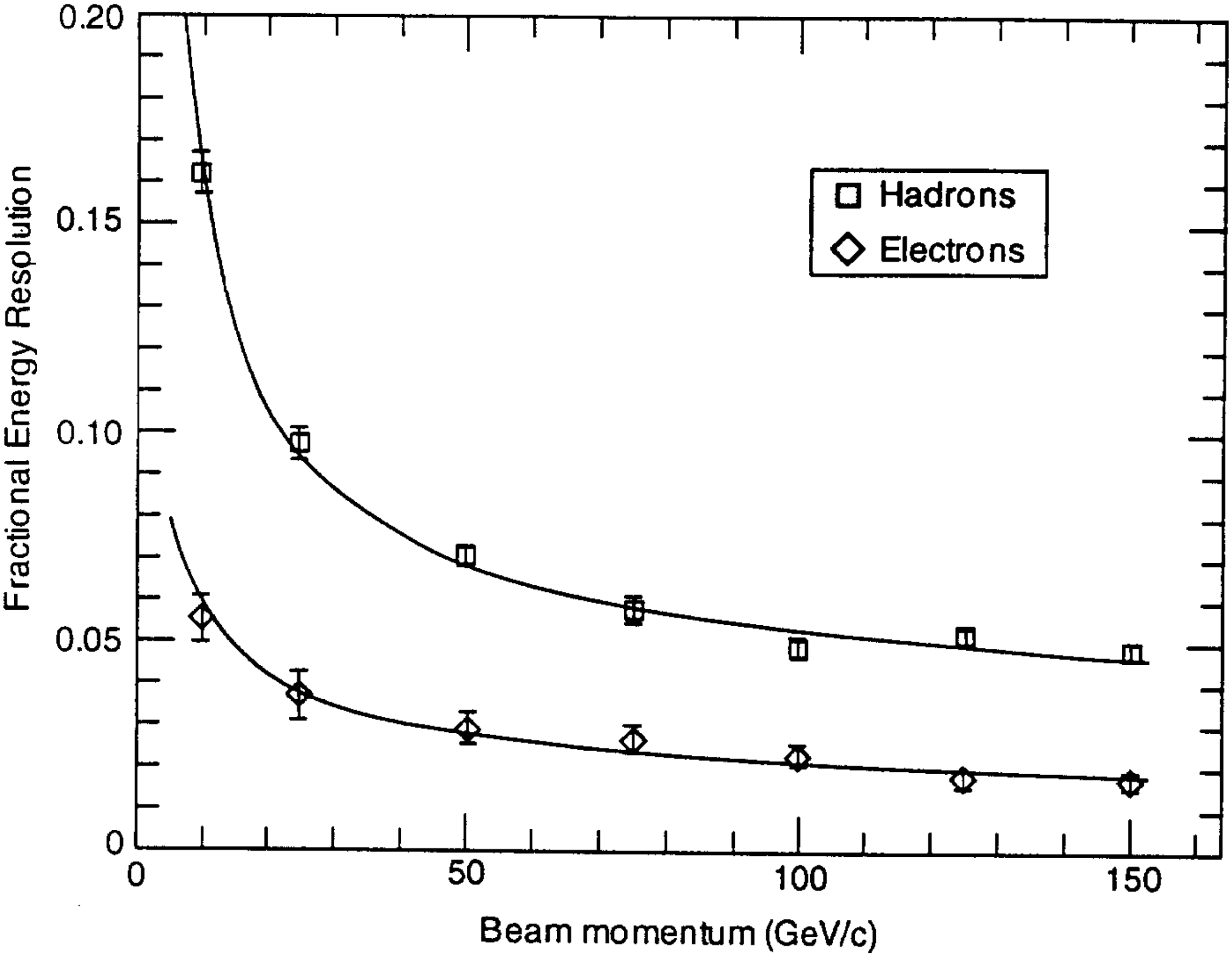

0.20
0.15
0.10
0.05
0
Fractional Energy Resolution
0
50
100
150
Beam momentum (GeV/c)
□ Hadrons
◇ Electrons

Figure 19

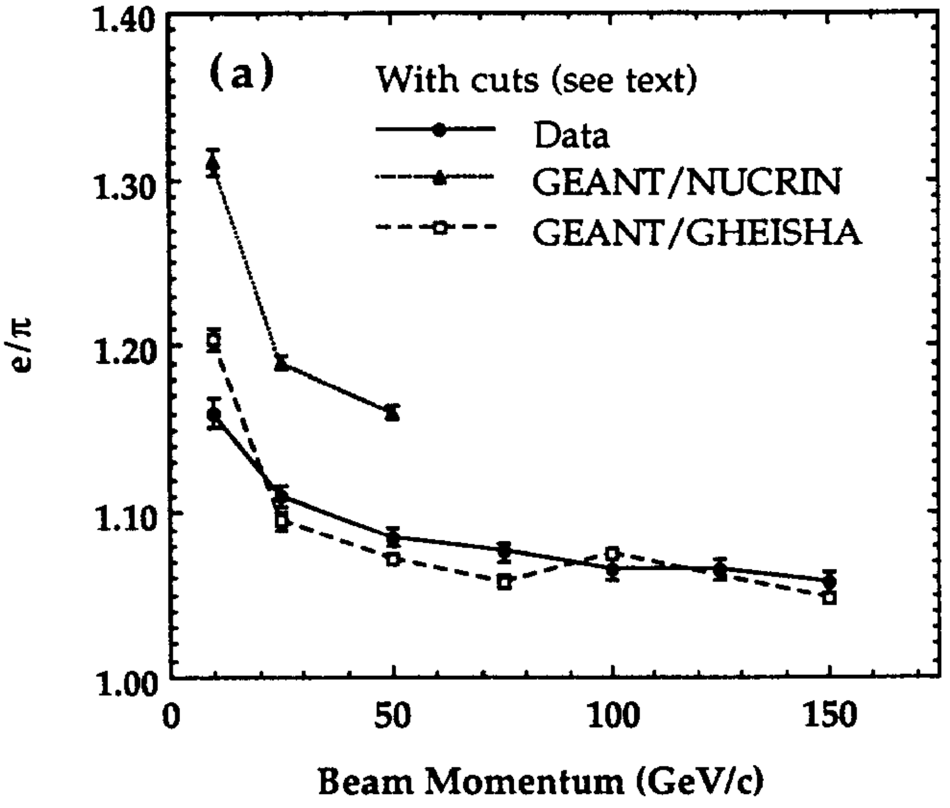
(a)
With cuts (see text)
Data
GEANT/NUCRIN
GEANT/GHEISHA
e/π
1.40
1.30
1.20
1.10
1.00
0
50
100
150
Beam Momentum (GeV/c)

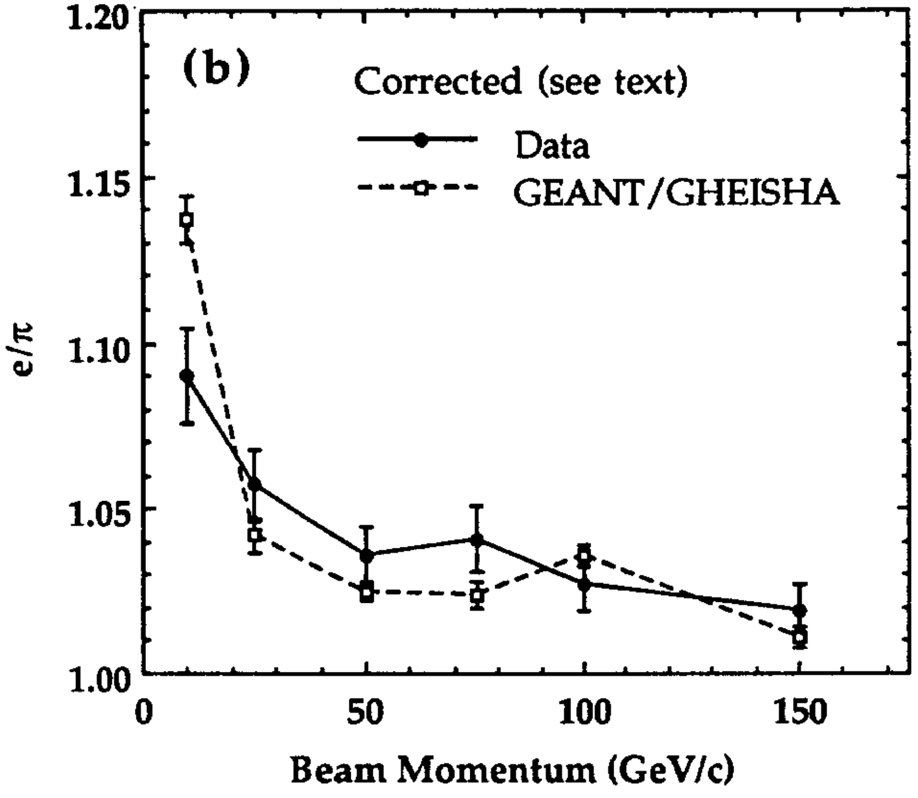
(b)
Corrected (see text)
Data
GEANT/GHEISHA
e/π
1.20
1.15
1.10
1.05
1.00
0
50
100
150
Beam Momentum (GeV/c)

Figure 20

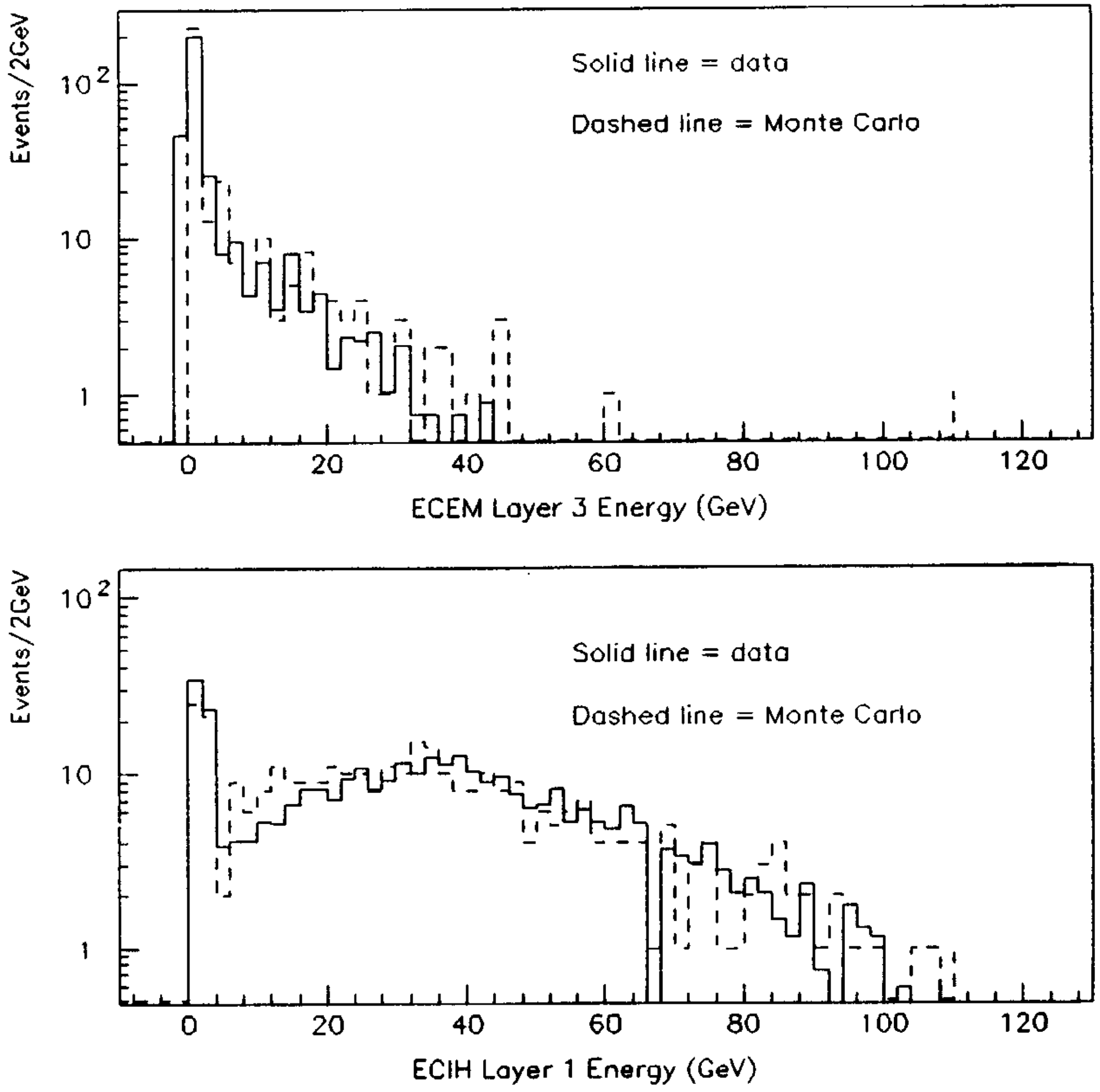
Events/2GeV
10^2
10
1
Solid line = data
Dashed line = Monte Carlo
0
20
40
60
80
100
120
ECEM Layer 3 Energy (GeV)
Events/2GeV
10^2
10
1
Solid line = data
Dashed line = Monte Carlo
0
20
40
60
80
100
120
ECIH Layer 1 Energy (GeV)

Figure 21

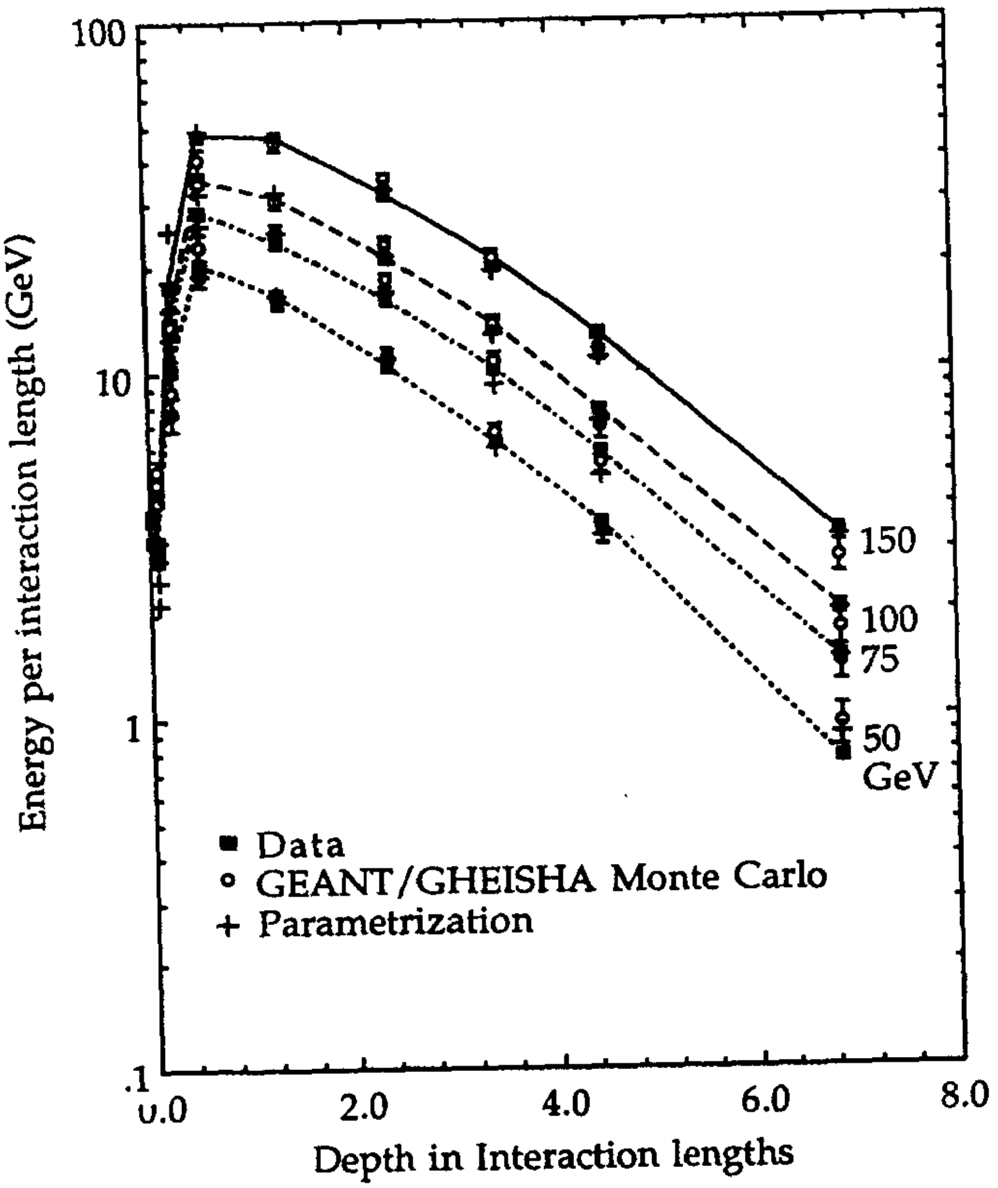
100
10
1
.1
0.0
2.0
4.0
6.0
8.0
Energy per interaction length (GeV)
Depth in Interaction lengths
150
100
75
50
GeV
■ Data
○ GEANT/GHEISHA Monte Carlo
+ Parametrization

Figure 22

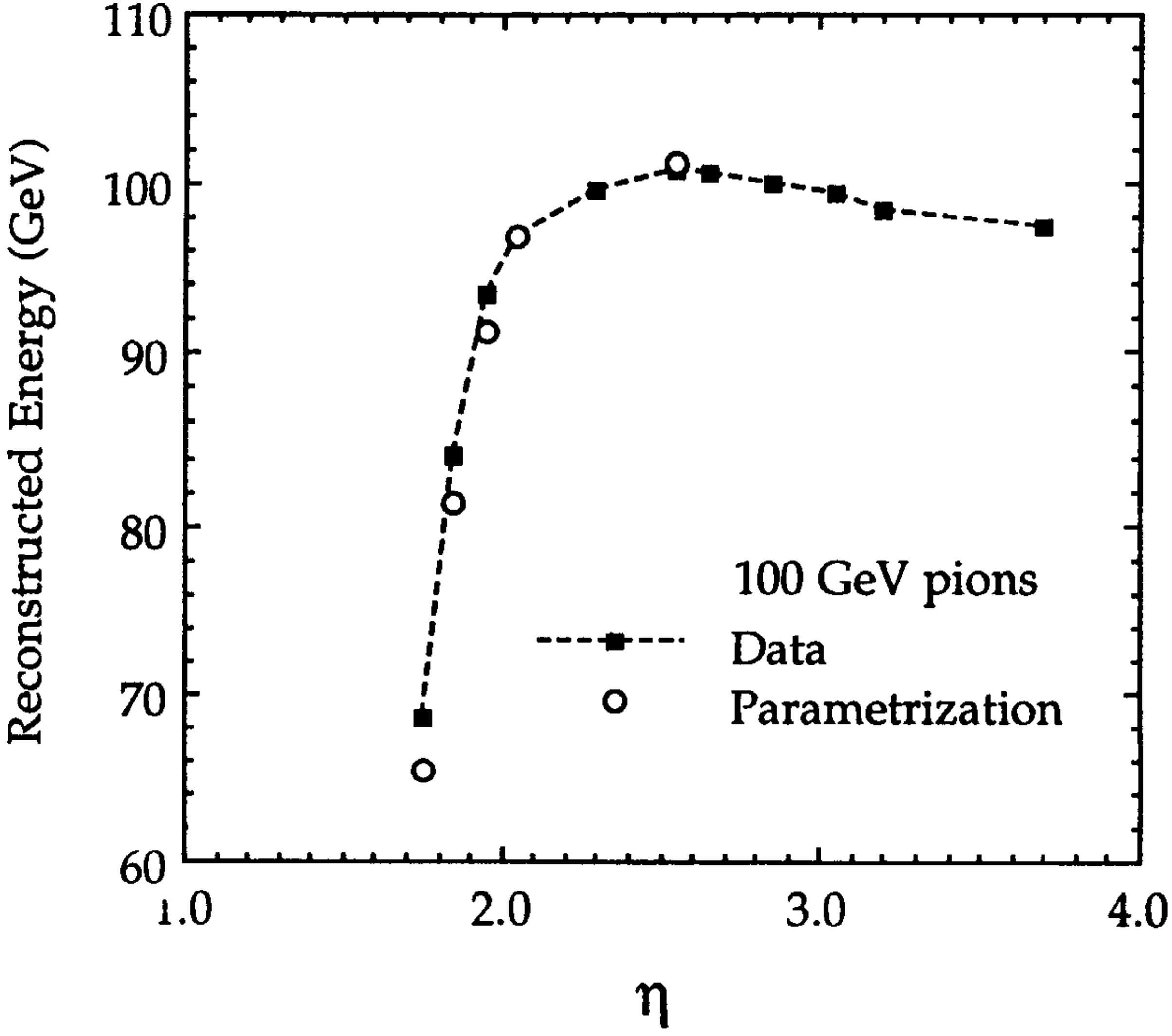
110
100
90
80
70
60
Reconstructed Energy (GeV)
1.0
2.0
3.0
4.0
η
100 GeV pions
Data
Parametrization

Figure 23

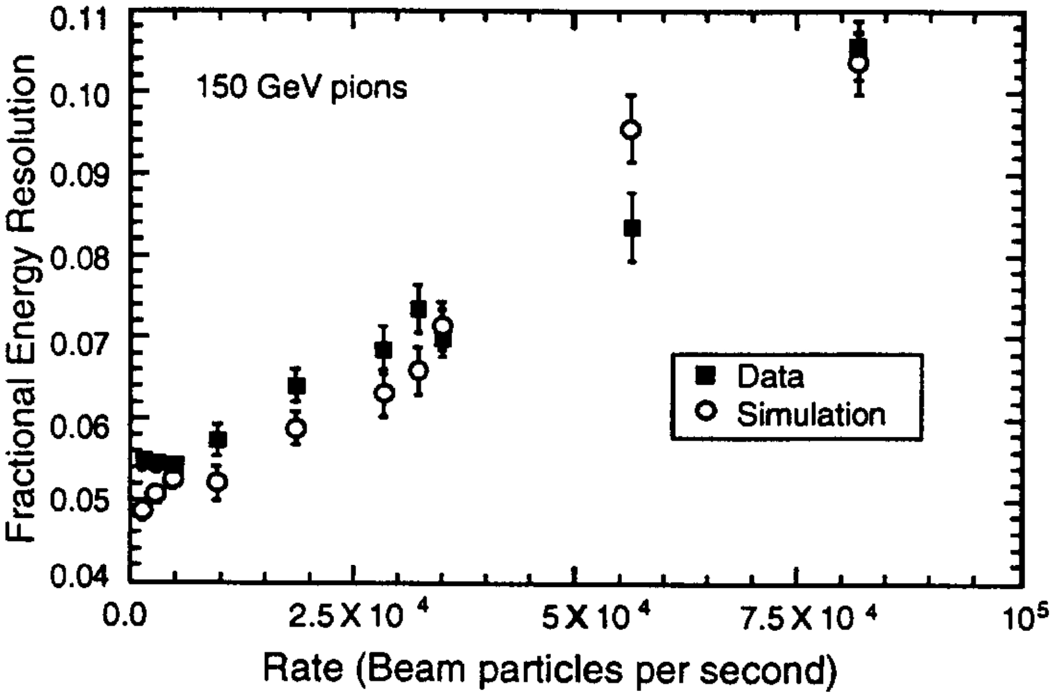

150 GeV pions
■ Data
○ Simulation
Fractional Energy Resolution
0.11
0.10
0.09
0.08
0.07
0.06
0.05
0.04
0.0
2.5 X 10 4
5 X 10 4
7.5 X 10 4
10⁵
Rate (Beam particles per second)

Figure 24

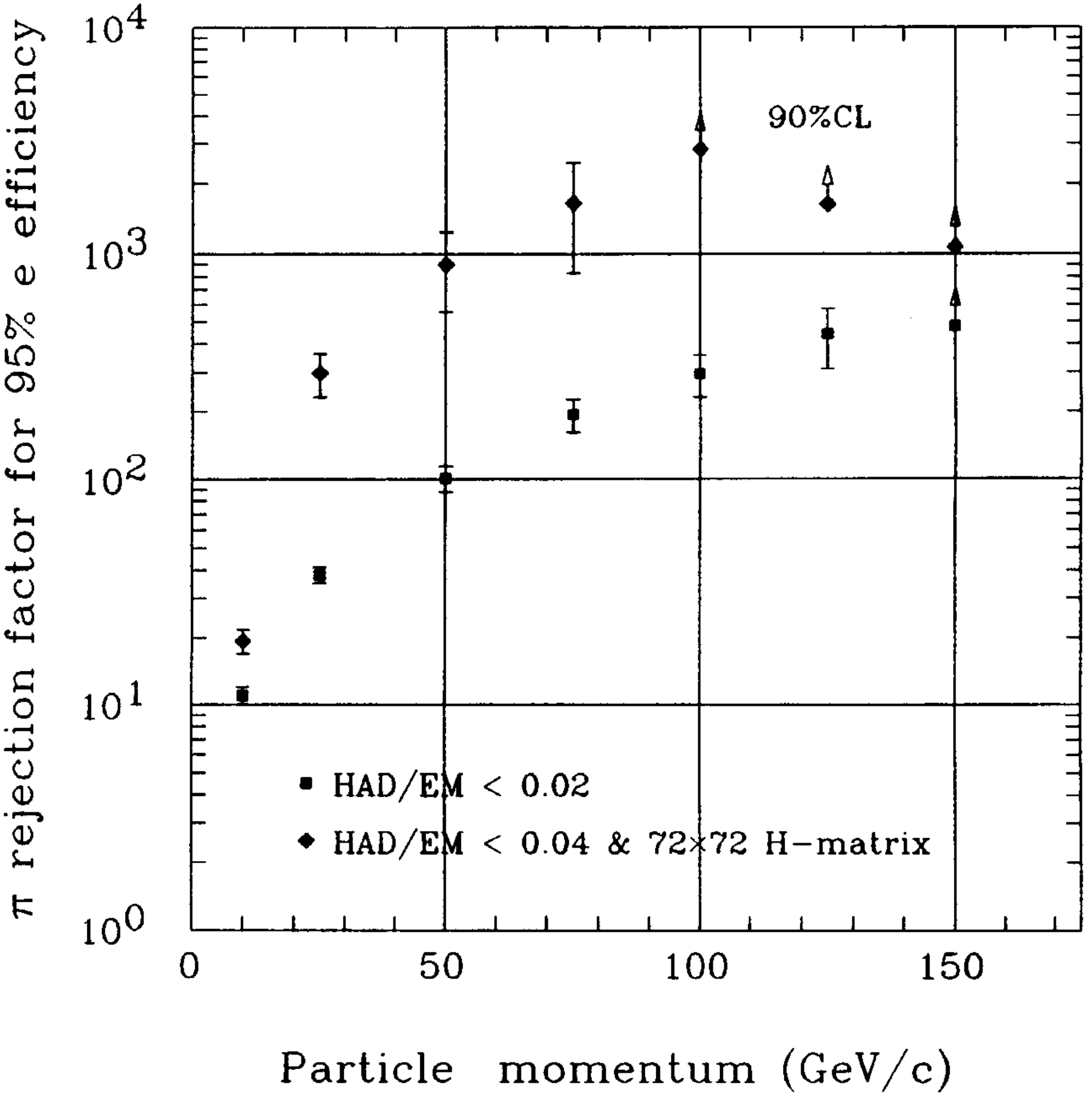

10^4
10^3
10^2
10^1
10^0
π rejection factor for 95% e efficiency
0
50
100
150
Particle momentum (GeV/c)
90%CL
■ HAD/EM < 0.02
◆ HAD/EM < 0.04 & 72×72 H−matrix

Figure 25

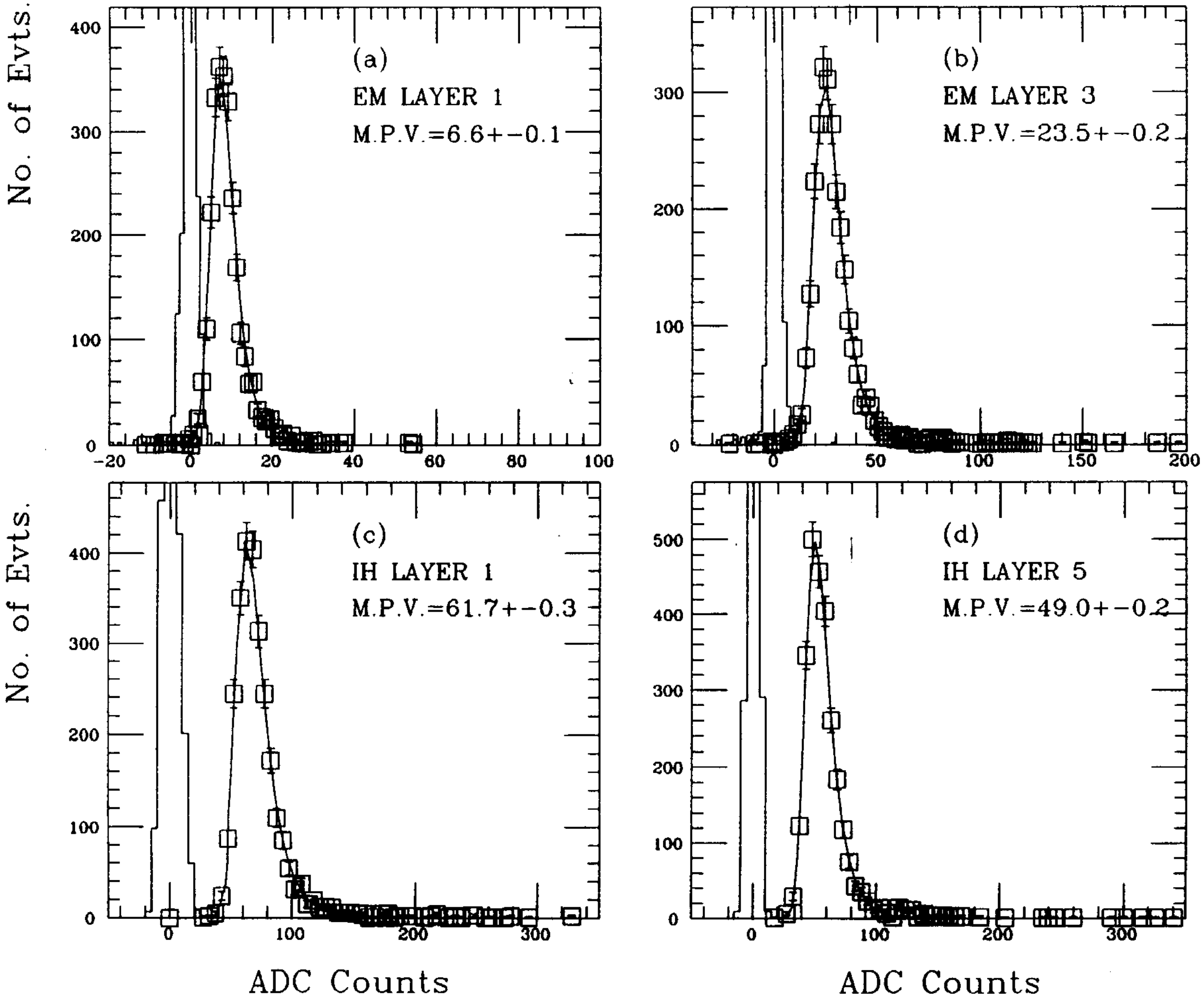
(a)
EM LAYER 1
M.P.V.=6.6+-0.1
(b)
EM LAYER 3
M.P.V.=23.5+-0.2
(c)
IH LAYER 1
M.P.V.=61.7+-0.3
(d)
IH LAYER 5
M.P.V.=49.0+-0.2
No. of Evts.
No. of Evts.
ADC Counts
ADC Counts
0
100
200
300
400
-20
0
20
40
60
80
100
0
100
200
300
0
50
100
150
200
0
100
200
300
400
0
100
200
300
0
100
200
300
400
500
0
100
200
300

Figure 26

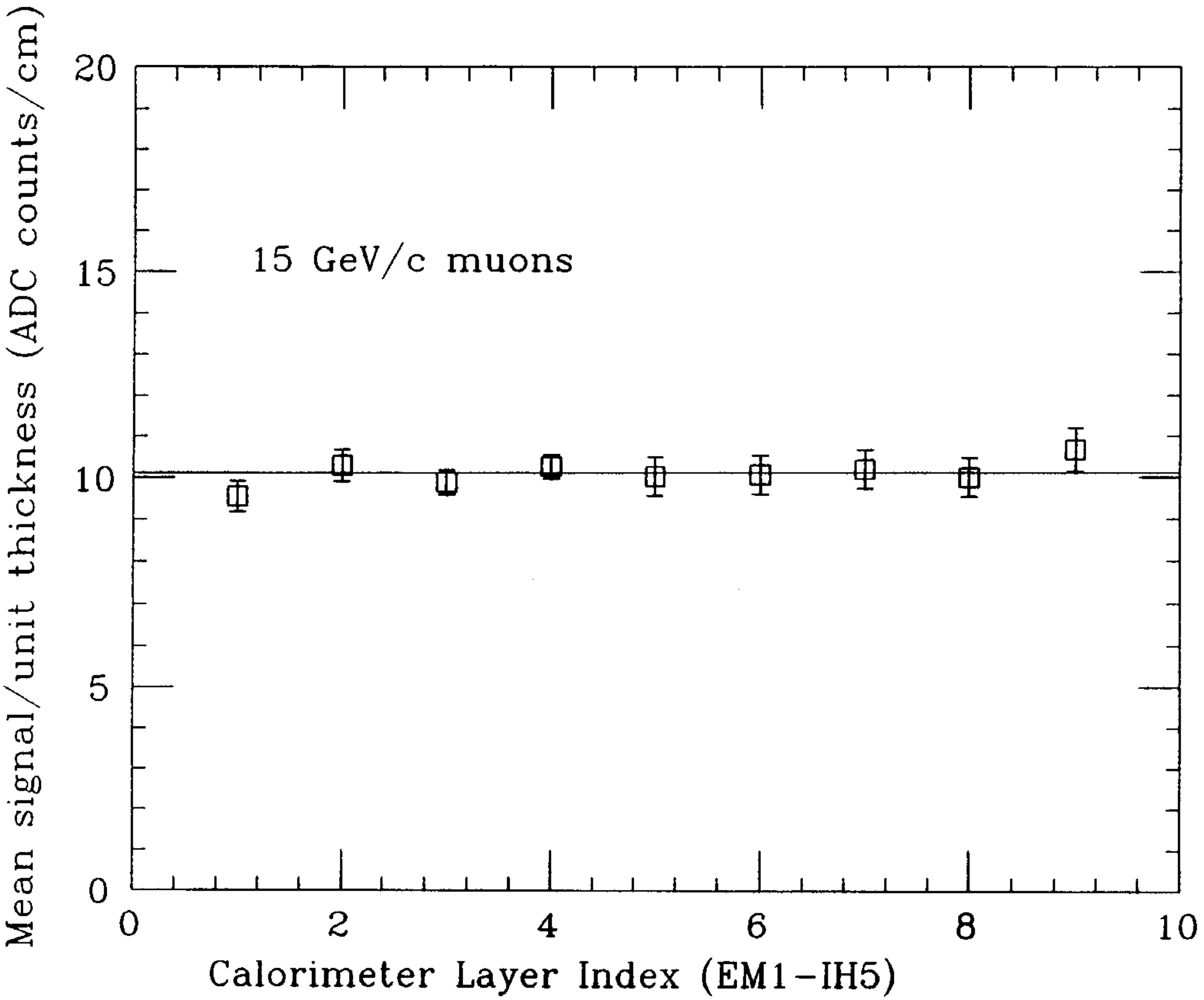

15 GeV/c muons
Mean signal/unit thickness (ADC counts/cm)
0
5
10
15
20
0
2
4
6
8
10
Calorimeter Layer Index (EM1-IH5)

Figure 27

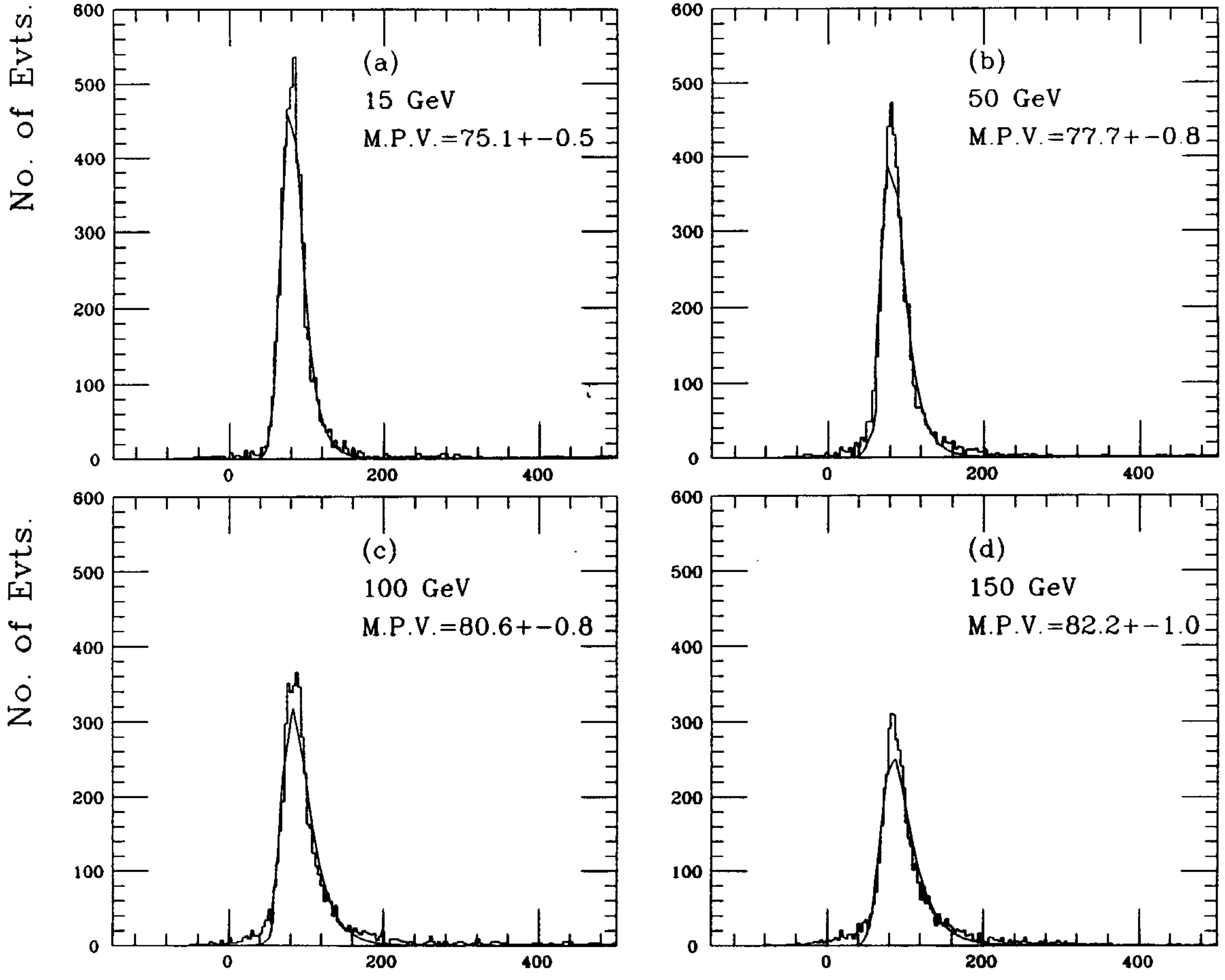
No. of Evts.
No. of Evts.
600
500
400
300
200
100
0
-0
200
400
ADC Counts
ADC Counts
(a)
15 GeV
M.P.V.=75.1+-0.5
(b)
50 GeV
M.P.V.=77.7+-0.8
(c)
100 GeV
M.P.V.=80.6+-0.8
(d)
150 GeV
M.P.V.=82.2+-1.0

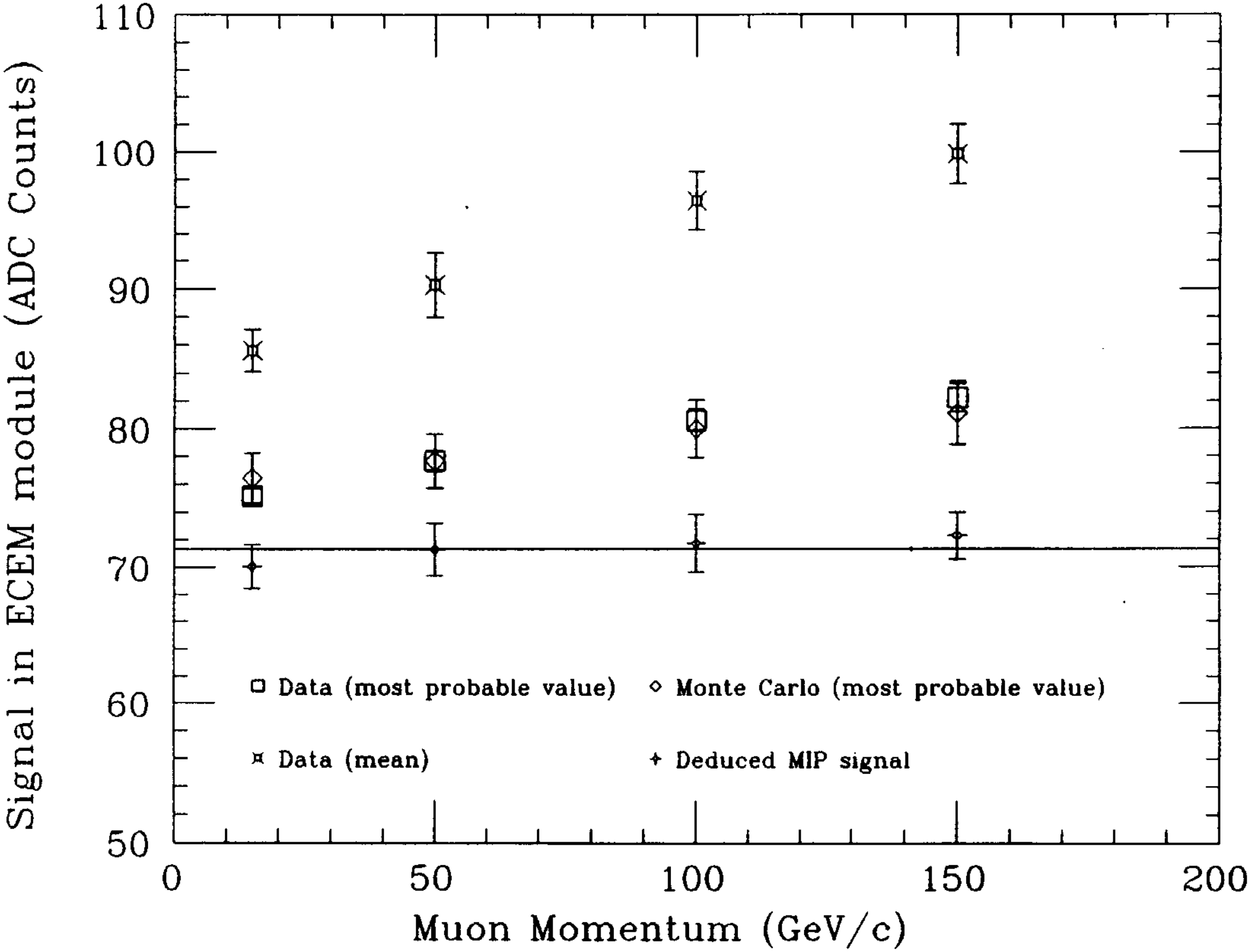
Signal in ECEM module (ADC Counts)
Muon Momentum (GeV/c)
110
100
90
80
70
60
50
0
50
100
150
200
□ Data (most probable value)
◇ Monte Carlo (most probable value)
⌑ Data (mean)
+ Deduced MIP signal

Figure 29

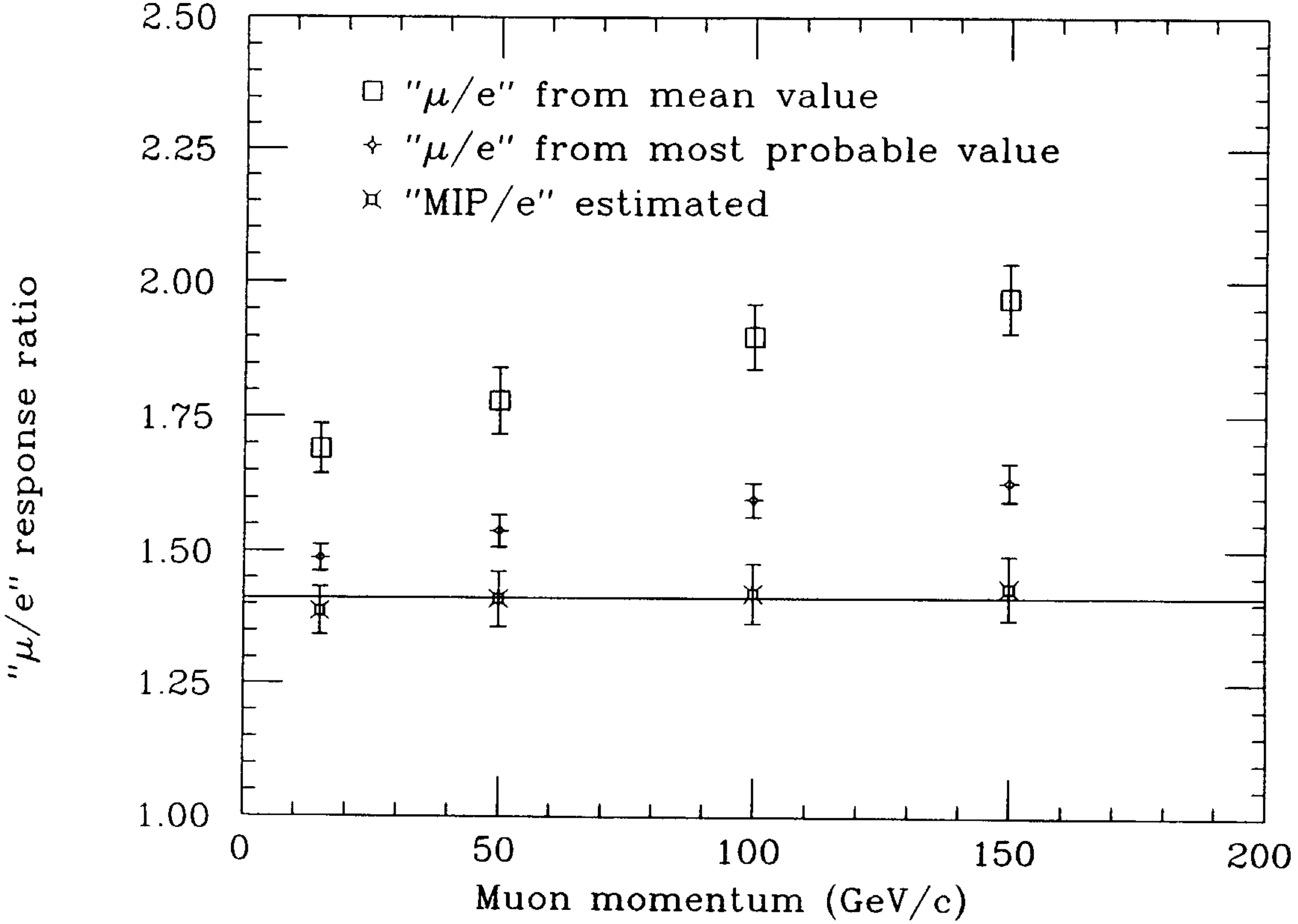

□ "μ/e" from mean value
✧ "μ/e" from most probable value
⌑ "MIP/e" estimated
"μ/e" response ratio
2.50
2.25
2.00
1.75
1.50
1.25
1.00
0
50
100
150
200
Muon momentum (GeV/c)

Figure 30